Mapping and classifying large deformation from digital imagery: application to analogue models of lithosphere deformation

Taco Broerse [1], Nemanja Krstekanić,[1,2] Cor Kasbergen[3] and Ernst Willingshofer[1]

[1]*Department of Earth Sciences, Faculty of Geosciences, Utrecht University, Utrecht, the Netherlands. E-mail: d.b.t.broerse@uu.nl*
[2]*Department of Regional Geology, Faculty of Mining and Geology, University of Belgrade, Belgrade, Serbia*
[3]*Faculty of Civil Engineering and Geosciences, Delft University of Technology, Delft, the Netherlands*

SUMMARY

Particle image velocimetry (PIV), a method based on image cross-correlation, is widely used for obtaining velocity fields from time-series of images of deforming objects. Rather than instantaneous velocities, we are interested in reconstructing cumulative deformation, and use PIV-derived incremental displacements for this purpose. Our focus is on analogue models of tectonic processes, which can accumulate large deformation. Importantly, PIV provides incremental displacements during analogue model evolution in a spatial reference (Eulerian) frame, without the need for explicit markers in a model. We integrate the displacements in a material reference (Lagrangian) frame, such that displacements can be integrated to track the spatial accumulative deformation field as a function of time. To describe cumulative, finite deformation, various strain tensors have been developed, and we discuss what strain measure best describes large shape changes, as standard infinitesimal strain tensors no longer apply for large deformation. PIV or comparable techniques have become a common method to determine strain in analogue models. However, the qualitative interpretation of observed strain has remained problematic for complex settings. Hence, PIV-derived displacements have not been fully exploited before, as methods to qualitatively characterize cumulative, large strain have been lacking. Notably, in tectonic settings, different types of deformation—extension, shortening, strike-slip—can be superimposed. We demonstrate that when shape changes are described in terms of Hencky strains, a logarithmic strain measure, finite deformation can be qualitatively described based on the relative magnitude of the two principal Hencky strains. Thereby, our method introduces a physically meaningful classification of large 2-D strains. We show that our strain type classification method allows for accurate mapping of tectonic structures in analogue models of lithospheric deformation, and complements visual inspection of fault geometries. Our method can easily discern complex strike-slip shear zones, thrust faults and extensional structures and its evolution in time. Our newly developed software to compute deformation is freely available and can be used to post-process incremental displacements from PIV or similar autocorrelation methods.

Key words: Continental tectonics: compressional; Continental tectonics: extensional; Continental tectonics: strike-slip and transform; Fractures, faults, and high strain deformation zones; Kinematics of crustal and mantle deformation; Mechanics, theory, and modelling.

1 INTRODUCTION

Determination of the cumulative strain of an object provides insight in the total shape change resulting from prolonged deformation, and aids in the characterization of the type of deformation leading to deformed structures. A technique such as particle image velocimetry (PIV) allows, by cross-correlating subsequent images, to obtain the incremental displacement field in between two time steps (e.g. Thielicke & Stamhuis (2014)). From these displacements, incremental deformation can be derived. Image cross-correlation can be used to observe displacements or deformation in physical analogue models of long-term tectonics. Applications range from mapping surface motions (Hampel *et al.* 2004), for the determination of strain in the horizontal plane (Boutelier & Oncken, 2011), or in side view (Cruz *et al.* 2008), for the imaging of

mantle flow in models (Funiciello *et al.* 2006). Similar correlation techniques are used to detect near step-wise displacements from coseismic deformation using optical satellite imagery (Kääb *et al.* 2017; Sotiris *et al.* 2018), SAR data (Morishita *et al.* 2017) or a combination of both (Lauer *et al.* 2020).

As PIV provides displacements in an Eulerian (i.e. space-fixed) reference frame, to integrate large cumulative deformations we need to convert these displacements to a Lagrangian (material-fixed) frame. Namely, we are primarily interested in the deformation of material, rather than the deformation at a location in space through which material advects. One can use the Eulerian displacements to follow material, provided that PIV-derived displacements are continuously available in time. Senatore *et al.* (2013) and (Stanier *et al.* 2016) show that PIV analysis of deformation of granular material allows for high resolution mapping of cumulative strain. Recently, Boutelier *et al.* (2019) illustrated the potential of integrated PIV displacements based on synthetic PIV results for simple shear zones, using appropriate finite strain descriptions.

As an alternative to PIV, displacement detection methods have been used that rely on tracing passive markers that are placed on models in a structured grid, manually (Schellart *et al.* 2003) or digitally (Fischer & Keating 2005; Cardozo & Allmendinger 2009; Duarte *et al.* 2013; Guillaume *et al.* 2013; Chen *et al.* 2015); for a review see section 5.3 of Schellart & Strak (2016). Tracking of passive markers provides Lagrangian displacements directly, but faults can be difficult to observe due to limited spatial resolution (Nilforoushan *et al.* 2008). PIV relies on the presence of contrasting texture of the study object in view, and potentially allows for a higher spatial resolution of the deformation field compared to methods where the deformation of an initially structured grid is traced through time. The achievable resolution depends mainly on the contrast and spatial brightness frequency of the surface texture and image resolution, where there is a trade-off between resolution and precision (White *et al.* 2003). PIV or similar autocorrelation techniques (digital volume correlation) can also be used to map displacements in 3-D, for example using X-ray tomography to visualize internal deformation of analogue models (Adam *et al.* 2013; Poppe *et al.* 2019), experiments on deformation of granular materials (Hall *et al.* 2010) or experimentally deformed rocks (Lenoir *et al.* 2007; Charalampidou *et al.* 2011; Mao & Chiang 2016). For transparent media, stereoscopic PIV has also proven itself to image 3-D velocity fields in subduction models (Strak & Schellart 2014). However, in our study we focus on 2-D deformation occurring in a horizontal plane, as our study materials are not transparant, and we use planar view images to determine deformation.

In this paper we seek to infer how the different types of tectonic deformation—extension, shortening and strike-slip—contribute to the cumulative deformation, documented through physical analogue modeling. A PIV-derived classification of the type of strain can so complement visual inspection of the type of faulting (e.g. as in Willingshofer & Sokoutis 2009), as well as determine distributed deformation in the absence of clear discrete faults.

When strains are small and rotations are negligible, such as holds for interseismic deformation measured using geodetic observations, the type of strain can be obtained using the ratio between the principal strains, such as used by Kreemer *et al.* (2014) for the interpretation of current day global deformation rates. For large strains this ratio no longer applies, as we show in Section 2.7. Studies have used derived quantities as maximum shear strains (Cruz *et al.* 2008) or vorticity (Adam *et al.* 2005) to resolve shear strain in vertical model cross-sections, or the first strain invariant to determine structures that deform under extension or shortening (Galland *et al.* 2016). To our knowledge, no existing method allows the simultaneous discrimination of extension, shortening and strike-slip (simple shear), or combinations of those.

In this paper we will discuss various deformation tensors that are common, infinitesimal strain, or less common in the geophysical modeling literature, finite strain and finite stretch. We will argue which tensors are best suited to describe large deformation and classify deformation. Based on a finite stretch tensor, we formulate a classification of deformation that can properly discern distributed or localized strike-slip, extension or shortening, or oblique combinations: transpression (strike-slip and orthogonal shortening) or transtension (strike-slip and orthogonal extension). Using both synthetic and analogue models of tectonic deformation, we will show that it is possible to create high resolution maps of finite strain and the type of strain.

2 DEFORMATION ANALYSIS

2.1 Material displacements from time-variable spatial displacements

Given incremental displacement vector fields in time, in our case obtained by particle image velocimetry (PIV, Thielicke & Stamhuis 2014), we want to determine the deformation field as a function of time. PIV provides the displacements in an Eulerian, space-fixed, undeformed, reference frame, which we want to express in a Lagrangian, material-fixed, deformed reference frame. In a Lagrangian frame, displacements refer to the particle path of material particles with respect to their initial positions. We define initial material points, from which we reconstruct particle paths through time, using the Eulerian displacements. The left panel of Fig. 1 shows these, virtual, initial material points. For the following time steps, material has advected, and these material points do no longer coincide with the PIV-derived Eulerian displacement points, see the middle panel. Similar as Senatore *et al.* (2013), Stanier *et al.* (2016), Boutelier *et al.* (2019), Krỳza *et al.* (2019) we calculate finite (i.e. cumulative) displacements by interpolating the Eulerian displacement fields.

The current location **x** of a point at epoch *t* that initially had the reference position **X** we construct as:

$$\mathbf{x} = \mathbf{X} + \sum_{i=1}^{t} \delta\mathbf{u}(\mathbf{X}, t),$$

(1)

interpolation spatial displacements
epoch 1

interpolation spatial displacements
epoch 2

particle paths after
6 epochs

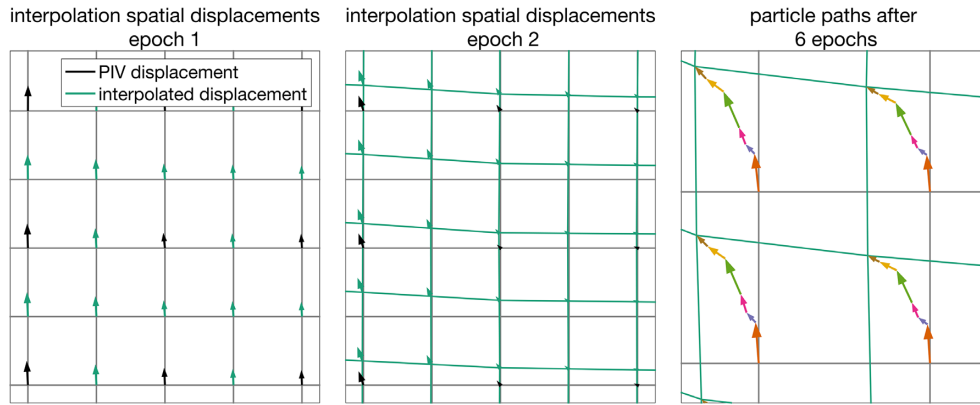— PIV displacement
— interpolated displacement

Figure 1. Interpolation of Eulerian displacements to follow material and construct a Lagrangian displacement field. Left-hand panel: PIV-derived Eulerian displacements (black arrows) and interpolated displacements (green arrows) on an initial material grid (black), representing virtual material points, at the first epoch. Middle panel: PIV-derived Eulerian displacements (black arrows) and initial grid (black) and interpolated displacements on the deformed material grid (green) at the second epoch. Right-hand panel: virtual particle paths from epochs 1 to 6, deforming, rotating and translating the initial grid (black) to the current deformed grid (green). The displacement field is based on data as used in Section 5.

where $\delta\mathbf{u}(\mathbf{X}, t)$ is the incremental Eulerian displacement at epoch t of the point that occupied position $\mathbf{X}$ in the reference state. We obtain $\delta\mathbf{u}(\mathbf{X}, t)$ by spatial bicubic spline interpolation (similarly as Stanier *et al.* 2016) as $\delta\mathbf{u}$ is provided on a regular grid by PIV. Fig. 1 shows how the original material frame has been deformed by incremental displacements, and how interpolated displacements can be used to construct particle paths. It is clear how for large deformation (i.e. translation, shape change, rotation) the Eulerian displacements quickly deviate from the Lagrangian material displacements. Extension and shortening that occur during observation lead to heterogeneity of the spatial resolution of the Lagrangian grid of virtual material points. A higher spatial resolution of the grid compared to the PIV displacement field can therefore be useful to mitigate progressive resolution loss in regions with large cumulative extension.

The procedure assumes that the PIV-derived velocities do not contain outliers. In this study we remove outliers based on a threshold displacement value as a function of the standard deviation of all displacement magnitudes (Thielicke & Stamhuis 2014), followed by a manual check of remaining outliers (that occur mainly during periods of sedimentation).

2.2 Deformation measures

Throughout this manuscript we use strain and stretch as measures to describe shape changes. As a simple 1-D scalar measure, extensional strain ϵ is:

$$\epsilon = \frac{L - L_0}{L_0} = \frac{\Delta L}{L_0} \tag{2}$$

with initial length L_0 and final length L. Extensional strain ϵ may stand here for both positive strain, as well as negative, shortening, strain. The range of possible 1-D strain values is [-1, ∞], with 0 denoting no deformation. In dimensions larger than 1, multiple definitions are possible for strain, depending on the reference frame and the magnitude of deformation (Sections 2.5.1 and 2.5.2). Stretch λ is a related measure that we will use frequently in this manuscript and that is defined as:

$$\lambda = \frac{L}{L_0} = \epsilon + 1, \tag{3}$$

where the stretch is always positive, and a stretch of 1 denotes no deformation. For purely extensional deformation stretch relates to strain as $\lambda = 1 + \epsilon$. Engineering shear strain γ is related to the change in angle ψ of two, originally, perpendicular lines:

$$\gamma = \tan(\psi). \tag{4}$$

In 2-D, stretches have a clear relation to the strain ellipse, where the two orthogonal principal stretches λ_1, λ_2 form the axes of the strain ellipse. The directions of these axes form principal axes, and along these directions the shape change can be defined by pure stretches (see Fig. 4). Finally, we will make use of the area ratio dA/dA_0 (i.e. dilatation from a 2-D perspective), which is a function of the principal stretches as:

$$dA/dA_0 = \lambda_1\lambda_2. \tag{5}$$

2.3 Deformation gradient

From the Lagrangian positions in time we derive the deformation gradient $\mathbf{F}$, a second order tensor that we will use later to derive all deformation measures such as strain and stretch. Fig. 2 shows the relation between old and new element vectors (i.e. any line within a small

$$dx = FdX$$

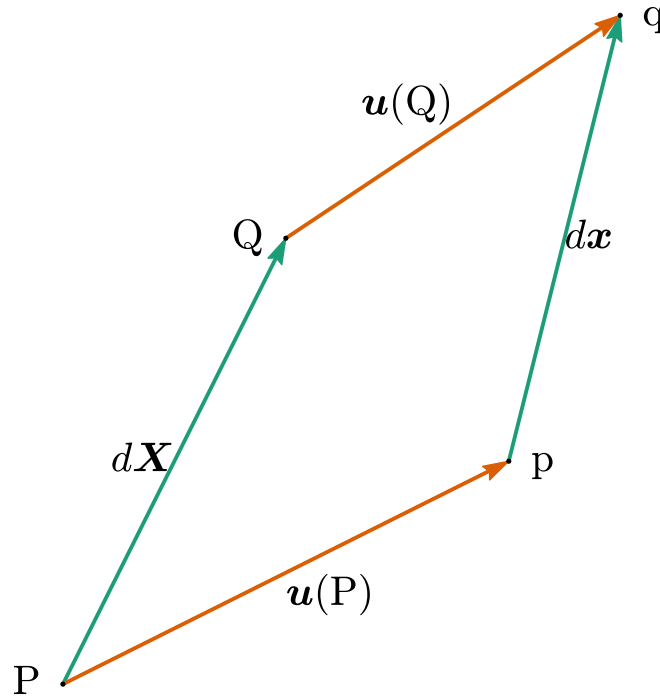**Figure 2.** The deformation gradient **F** relates the deformed state to the undeformed state. A material vector $d\mathbf{X}$ that runs from point P to Q (i.e. a side of a small material element) in the original configuration, to the material vector in the deformed configuration $d\mathbf{x}$, with the material that first occupied points P and Q now in points p and q. Displacement vectors $u(P)$ and $u(Q)$ provide the displacements between the two states.

unit of material) and displacements. The deformation gradient relates initial vectors of the undeformed material $d\mathbf{X}$ to the deformed, final material vector $d\mathbf{x}$, by (Malvern 1969):

$$d\mathbf{x} = \mathbf{F}d\mathbf{X} \qquad (6)$$

This means that the components of deformation gradient tensor are defined as:

$$\mathbf{F} = \frac{\partial \mathbf{x}}{\partial \mathbf{X}}. \qquad (7)$$

We can write the displacement **u** as the difference between current and reference coordinates:

$$\mathbf{u} = \mathbf{x} - \mathbf{X}. \qquad (8)$$

Thus, the deformation gradient can be reformulated as a function of the displacements:

$$\mathbf{F} = \frac{\partial}{\partial \mathbf{X}}(\mathbf{X} + \mathbf{u}) = \mathbf{I} + \frac{\partial \mathbf{u}}{\partial \mathbf{X}} = \mathbf{I} + \nabla \mathbf{u}. \qquad (9)$$

Here $\frac{\partial \mathbf{u}}{\partial \mathbf{X}}$ or $\nabla \mathbf{u}$ is the gradient of the displacement vector field, and **I** is the identity matrix, which represents the current state. This means that the deformation gradient is a simple relation of the partial derivative of the displacement with respect to the reference coordinates. In 2-D the deformation gradient becomes:

$$\mathbf{F} = \begin{bmatrix} 1 + \frac{\partial u_X}{\partial X} & \frac{\partial u_X}{\partial Y} \\ \frac{\partial u_Y}{\partial X} & 1 + \frac{\partial u_Y}{\partial Y} \end{bmatrix} \qquad (10)$$

When we regard the deformation as a product of rigid body rotation and translation and distortion, **F** captures all except the rigid body translation, as rigid body translations do not lead to gradients in displacements.

Computation of the deformation gradient

In eq. (1) we have discussed the coordinates of points of which we have tracked the change in coordinates **x**. For the following, we define quadrilateral elements (that in our implementation starts as squares in the undeformed state) and we apply the computation of **F** to these elements. We make use of linear shape functions to determine the partial derivatives of the displacement $\frac{\partial \mathbf{u}}{\partial \mathbf{X}}$ (see Appendix A).
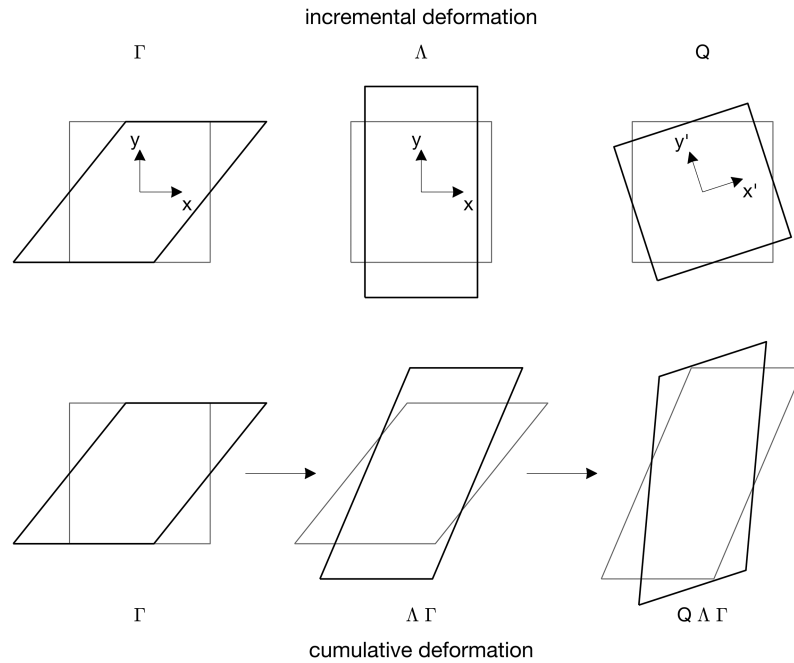
Figure 3. Any homogeneous deformation **F** can be written as a succession of a simple shear parallel to x Γ; an extension in x and an extension in y direction Λ; followed by an orthogonal rotation **Q** (Srinivasa 2012). Here, the change between initial line vectors $d\mathbf{X}$ (in this case the side vectors of a square) to final initial line vectors $d\mathbf{x}$ (the deformed quadrilaterals) is determined by: $d\mathbf{x} = \mathbf{F}d\mathbf{X}$. First row, incremental deformation, second row, cumulative deformation.

2.4 General deformation described with the deformation gradient

Any deformation that can be described by **F**, can be written as a serial combination of a simple shear, simple extensions along the x or y axes and a rotation (Srinivasa 2012):

$$\mathbf{F} = \mathbf{Q}\tilde{\mathbf{F}}. \tag{11}$$

Distortion $\tilde{\mathbf{F}}$ contains all shape changes and **Q** is an orthogonal rotation matrix ($\mathbf{Q}^T\mathbf{Q} = \mathbf{I}$). The distortion can very conveniently be written as a successive multiplication of first a shearing motion followed by a biaxial extension (Freed *et al.* 2019):

$$\tilde{\mathbf{F}} = \Lambda\Gamma = \begin{bmatrix} a & 0 \\ 0 & b \end{bmatrix} \begin{bmatrix} 1 & \gamma \\ 0 & 1 \end{bmatrix} = \begin{bmatrix} a & a\gamma \\ 0 & b \end{bmatrix}. \tag{12}$$

Fig. 3 shows an example of the resulting deformation with applying distortion and rotation. For example, shearing (simple shear) parallel to x can be achieved by engineering strain $\gamma \neq 0$. Subsequently, extension or shortening along x can be achieved with stretch parameter $a > 1$ and $0 < a < 1$, respectively. Similarly extension along y can be achieved using stretch parameter $b \neq 1$. Finally, rotation matrix **Q** rotates the Cartesian reference frame **x** under a counter-clockwise angle θ to the new coordinates $\mathbf{x}'$: $\mathbf{x}' = \mathbf{Q}\mathbf{x}$. With the rotation given by:

$$\mathbf{Q} = \begin{bmatrix} cos(\theta) & -sin(\theta) \\ sin(\theta) & cos(\theta) \end{bmatrix} \tag{13}$$

We will use the formulation of the distortion $\tilde{\mathbf{F}}$ in Section 2.7 to classify large shape changes (distortion) as combinations of shearing and extensions.

2.5 Strain and stretch tensors

Different measures have been derived to uniquely decompose the deformation described by **F** into rotations and shape changes. We discuss a few of these and argue which of these tensors are best suited to quantitatively describe large changes in shape.

2.5.1 Small deformation: infinitesimal strain

For small deformations, the product of successive deformations (see eqs 11 and 12) can be approximated by a sum of successive deformations. In that case, we can write the deformation gradient as the sum of the current state **I**, shape changes $\boldsymbol{\epsilon}$ and rotation $\boldsymbol{\omega}$ (Allmendinger *et al.* 2011):

$$\mathbf{F} = \mathbf{I} + \boldsymbol{\epsilon} + \boldsymbol{\omega}. \tag{14}$$

Shape changes ϵ are expressed in terms of strain, a quantity closely related to the 1-D extension ϵ (eq. 2). When rotations ω—due to rigid body rotations as well as due to shear—are small, we can describe shape changes using the Lagrangian infinitesimal strain tensor ϵ (in 2-D, Malvern 1969):

$$\epsilon = \begin{bmatrix} \epsilon_{xx} & \epsilon_{xy} \\ \epsilon_{xy} & \epsilon_{yy} \end{bmatrix} = \begin{bmatrix} \frac{\partial u_x}{\partial X} & \frac{1}{2}\left(\frac{\partial u_x}{\partial Y} + \frac{\partial u_y}{\partial X}\right) \\ \frac{1}{2}\left(\frac{\partial u_x}{\partial Y} + \frac{\partial u_y}{\partial X}\right) & \frac{\partial u_y}{\partial Y} \end{bmatrix} \tag{15}$$

with normal extensions ϵ_{xx} and ϵ_{yy} on the diagonals and the shear term ϵ_{xy} on the off-diagonals. The infinitesimal strain tensor can be written as a function of the displacement tensor $\nabla\mathbf{u}$, and thus can be easily computed from the deformation gradient ($\mathbf{F} = \mathbf{I} + \nabla\mathbf{u}$) as:

$$\epsilon = \frac{1}{2}\left(\nabla\mathbf{u} + (\nabla\mathbf{u})^T\right) = \frac{1}{2}\left(\mathbf{F} + \mathbf{F}^T\right) - \mathbf{I}. \tag{16}$$

Complementary to the strain tensor is the rotation tensor ω, which relates to the displacement tensor and strain as $\nabla\mathbf{u} = \epsilon + \omega$. For straight material lines in deforming elements, the rotation differs depending on the orientation and ω represents the average rotation, integrated over all orientations of a small piece of material and is defined as:

$$\omega = \begin{bmatrix} 0 & -\omega \\ \omega & 0 \end{bmatrix} = \begin{bmatrix} 0 & \frac{1}{2}\left(\frac{\partial u_x}{\partial Y} - \frac{\partial u_y}{\partial X}\right) \\ \frac{1}{2}\left(\frac{\partial u_y}{\partial X} - \frac{\partial u_x}{\partial Y}\right) & 0 \end{bmatrix} \tag{17}$$

which can also be written as a function of the deformation gradient:

$$\omega = \frac{1}{2}\left(\nabla\mathbf{u} - (\nabla\mathbf{u})^T\right) = \frac{1}{2}\left(\mathbf{F} - \mathbf{F}^T\right). \tag{18}$$

Example: small strains, rotation and shear

The infinitesimal strain expression (eq. 15) only makes sense as long as rotations are small, as rotations will affect the diagonal elements of ϵ, even in the absence of shape changes. For an object under rigid body rotation with counter-clockwise angle θ ($a = 1$, $b = 1$, $\gamma = 0$), the deformation gradient is:

$$\mathbf{F}_{\text{rot}} = \mathbf{Q} = \begin{bmatrix} \cos(\theta) & -\sin(\theta) \\ \sin(\theta) & \cos(\theta) \end{bmatrix}. \tag{19}$$

Even in the absence of shape changes the infinitesimal strain then becomes non-zero, which demonstrates the physical insignificance of ϵ to describe shape changes when $\cos(\theta)$ is no longer approximately 1:

$$\epsilon_{\text{rot}} = \begin{bmatrix} \cos(\theta) - 1 & 0 \\ 0 & \cos(\theta) - 1 \end{bmatrix}. \tag{20}$$

A second case: for a material subject to simple shear, with shear parallel to x ($a = 1$, $b = 1$, $\gamma > 0$, $\theta = 0$), the deformation gradient is:

$$\mathbf{F}_{\text{ss}} = \Gamma = \begin{bmatrix} 1 & \gamma \\ 0 & 1 \end{bmatrix} \tag{21}$$

and the infinitesimal shear becomes:

$$\epsilon_{\text{ss}} = \begin{bmatrix} 0 & \gamma/2 \\ \gamma/2 & 0 \end{bmatrix}. \tag{22}$$

Material that originally is parallel with the y-axis will elongate, due to the shear parallel to x, see the left-hand panel of Fig. 3. However, this effect is absent in the infinitesimal strain, as ϵ_y is zero. For small strains this elongation along y may be small, and can thus be neglected. But it will become significant for large shears (shown in Section 2.5.4). For objects undergoing large deformation, the infinitesimal strain description can thus only be used for small cumulative rotations and small shears (we investigate in Section 2.5.4 when shear can no longer be considered small). Notably, the summation of incremental strains is only possible when the principal strain axes do not change during deformation (Malvern 1969), which again rules out application for materials subject to shear or rigid body rotations.

2.5.2 Large deformation: finite strain

For large deformations there are different strain definitions that are insensitive to rotations, and include extension resulting from shear on diagonal components of strain. Finite strain is related to the squared length change, see for a derivation Malvern (1969) or Allmendinger *et al.* (2011). For large strains it matters whether the strain is described with respect to the undeformed state $\mathbf{E}$—Lagrange–Green strain tensor—or, with respect to the deformed state $\mathbf{E}^*$ —Almansi–Green strain tensor:

$$\mathbf{E} = \frac{1}{2}\left(\mathbf{F}^T\mathbf{F} - \mathbf{I}\right) = \frac{1}{2}\left(\mathbf{C} - \mathbf{I}\right) \tag{23}$$

$$\mathbf{E}^* = \frac{1}{2}\left(\mathbf{F}\mathbf{F}^T - \mathbf{I}\right) = \frac{1}{2}\left(\mathbf{B} - \mathbf{I}\right) \tag{24}$$

with right Cauchy–Green deformation tensor $\mathbf{C}$ and left Cauchy–Green deformation tensor $\mathbf{B}$. The components of finite strain tensors $\mathbf{E}$ and $\mathbf{E}^*$ read (Malvern [1969](#)):

$$E_{ij} = \frac{1}{2}\left(\frac{\partial u_i}{\partial X_j} + \frac{\partial u_j}{\partial X_i} + \frac{\partial u_k}{\partial X_i}\frac{\partial u_k}{\partial X_j}\right) \tag{25}$$

$$E_{ij}^* = \frac{1}{2}\left(\frac{\partial u_i}{\partial x_j} + \frac{\partial u_j}{\partial x_i} - \frac{\partial u_k}{\partial x_i}\frac{\partial u_k}{\partial x_j}\right). \tag{26}$$

The Lagrange–Green strain tensor contains partial derivatives with respect to the reference coordinates $\mathbf{X}$ while the Almansi–Green strain tensor has partial derivatives with respect to the current coordinates $\mathbf{x}$. When the off-diagonal terms of $\mathbf{F}$ are small, $\mathbf{E}$ and $\mathbf{E}^*$ reduce to the infinitesimal strain tensor $\boldsymbol{\epsilon}$ (eq. [15](#)). The finite strain tensors are insensitive to rigid body rotations as $\mathbf{C} = \mathbf{F}^T\mathbf{F} = \left(\mathbf{Q}\tilde{\mathbf{F}}\right)^T\mathbf{Q}\tilde{\mathbf{F}} = \tilde{\mathbf{F}}^T\mathbf{Q}^T\mathbf{Q}\tilde{\mathbf{F}} = \tilde{\mathbf{F}}^T\tilde{\mathbf{F}}$.

Example: non-proportionality of principal finite strains with length change

The large strain tensors have the advantage that shear-induced extension is accounted for, but they have the drawback that principal strains are not proportional with length change. For uniaxial extension ($a > 1, b = 1, \gamma > 0, \theta = 0$), $\mathbf{F} = \boldsymbol{\Lambda}$, and the Almansi strain tensor becomes:

$$\mathbf{E}_{ue}^* = \begin{bmatrix} \frac{a^2}{2} - \frac{1}{2} & 0 \\ 0 & 0 \end{bmatrix}. \tag{27}$$

Hence, in the x-direction there is a finite strain (E_{xx}^*) that is not proportional to the stretch: $\lambda = 1 + \epsilon = a \neq E_{xx}^* + 1$. Still, the principal finite strains E_1^* can be related to principal stretch by $\lambda_i = \sqrt{1 + 2E_i^*}$ (Malvern [1969](#)), but more intuitive deformation tensors can prove more useful (see the next section).

2.5.3 Large deformation: finite stretch

Instead of measures for strain, we make use of stretch tensors that are a decomposition of the deformation gradient $\mathbf{F}$. Whereas for small deformation, rotation $\boldsymbol{\omega}$ and strain $\boldsymbol{\epsilon}$ can be summed (eq. [14](#)), for large deformation we can no longer assume that shapes stay approximately constant after applying subsequent deformations (i.e. $\mathbf{x} \not\approx \mathbf{X}$). Thus, instead of a summation as in Section 2.5.1, the deformation gradient $\mathbf{F}$ can be written as a product of a rotation $\mathbf{R}$ (an orthogonal rotation tensor: $\mathbf{R}\mathbf{R}^T = \mathbf{I}$) and a symmetric, stretch tensor with positive principal values (Malvern [1969](#)). Thereby $\mathbf{R}$ has the form of the rotation matrix $\mathbf{Q}$ (eq. [13](#)) that applies a rotation with angle θ. Depending on the order of multiplication of rotation and stretching we can write $\mathbf{F}$ as:

$$\mathbf{F} = \mathbf{R}\mathbf{U} = \mathbf{V}\mathbf{R} \tag{28}$$

Here $\mathbf{U}$ is called the right stretch tensor and $\mathbf{V}$ is the left stretch tensor. Fig. [4](#) shows how $\mathbf{U}$ describes the shape change in the unrotated state (the original configuration) while $\mathbf{V}$ provides the shape change after applying the rotation. Hence, $\mathbf{V}$ represents the shape change in the final state, which is why it is our stretch tensor of choice. $\mathbf{U}$ and $\mathbf{V}$ are related to the Cauchy-Green deformation tensors (eq. [23](#)) by:

$$\mathbf{U} = \sqrt{\mathbf{C}} \qquad \mathbf{V} = \sqrt{\mathbf{B}} \tag{29}$$

$\mathbf{U}$ and $\mathbf{V}$ have the same principal values λ_i, and these are related to the principal values μ_i of $\mathbf{C}$ and $\mathbf{B}$ by $\lambda_i = \sqrt{\mu_i}$. The direction of the principal axes of $\mathbf{U}$ and $\mathbf{V}$ are however different, due to the rotation of $\mathbf{R}$, see Fig. [4](#). $\mathbf{U}$ and $\mathbf{V}$ are computed by polar decomposition, for which we apply the Hoger & Carlson ([1984](#)) algorithm that provides a closed form solution, see appendix B. Because $\mathbf{U}$ and $\mathbf{V}$ are decompositions of $\mathbf{F}$, the principal finite stretches are proportional to length changes (as is not the case for finite strain, see previous section). Principal stretches represent the extension in the principal directions, and are in the range $[0, \infty]$, with values smaller than 1 denoting shortening and values larger than 1 extension. Because the stretch tensors $\mathbf{U}$ and $\mathbf{V}$ are symmetric, simple shear will introduce rotations, even in the absence of proper rigid body rotations. $\mathbf{R}$ describes the mean rotation, i.e. averaged over all material line orientations $[0, 2\pi]$.

Interpretation of the stretch tensor

In 2-D, the left-stretch tensor has the form:

$$V = \begin{bmatrix} V_{xx} & V_{xy} \\ V_{xy} & V_{yy} \end{bmatrix}. \tag{30}$$

While the tensor components of $\mathbf{V}$ denote extensional (diagonal components) and shearing (off-diagonal components) deformation, the individual tensor components are of limited use for intuitive interpretation of deformation, especially if rotation angle θ (of $\mathbf{R}$) is large. Because $\mathbf{V}$ is preceded by rotation $\mathbf{R}$ (eq. [28](#)), the deformation described by $\mathbf{V}$ does not apply to material that was in the undeformed state
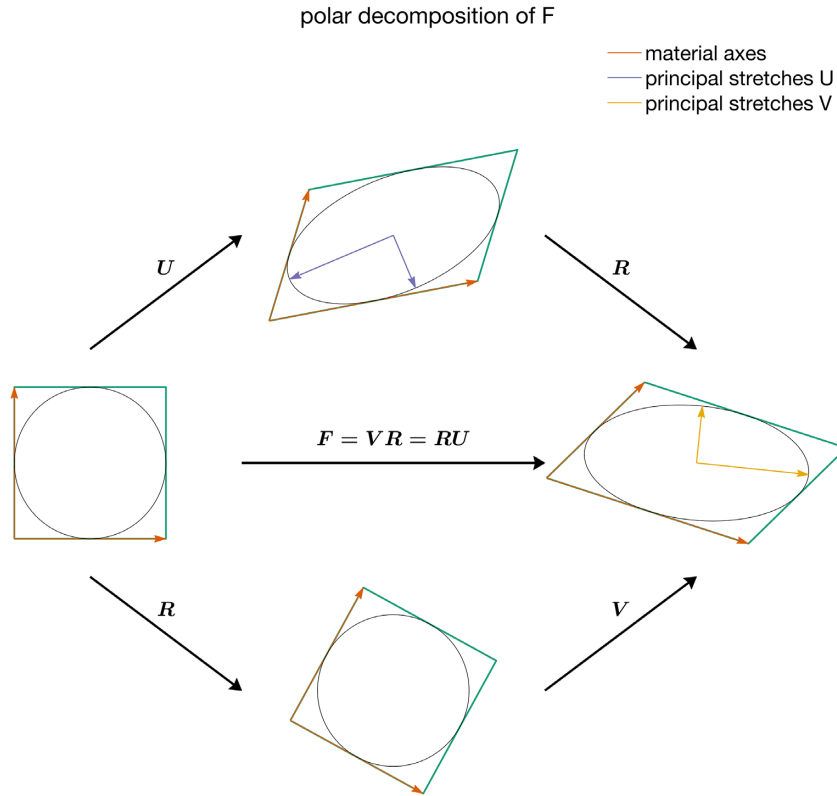
polar decomposition of F

Figure 4. Sketch of the polar decomposition of the deformation gradient **F** into an orthogonal rotation **R** and symmetric stretch tensors **V** or **U**. Here we apply the deformation of **F** to an initially square material element, with side vectors $d\boldsymbol{X}$. The deformed configuration (right) leads to an element with side vectors $d\mathbf{x} = \mathbf{F}d\mathbf{X}$. The decomposition can be written as first a stretch **U** followed by a rotation **R**, or first a rotation **R** followed by a stretch **V**. Principal stretches λ of **V** provide the stretch in the final, deformed, configuration, whereas stretches λ of **U** provide the stretch in the original configuration. Material axes provide reference for the reader. We also show strain ellipses in black, that can be constructed using circle coordinates as $d\boldsymbol{X}$. Principal stretches form the axes of the strain ellipse, where the principal vectors of **V** construct a strain ellipse in the final state. Because **V** and **U** are symmetric tensors, the rotation angle of **R** is non-zero for simple shear contributions.

oriented along *X* or *Y*, but rather to the material that is oriented along *X* or *Y* after the rotation by **R** (Fig. 4). The same arguments hold for **U**, where the rotation by **R** follows after the deformation under **U**.

From a kinematic perspective, we prefer to represent the stretch tensors not in the chosen reference coordinate system, which may be arbitrarily oriented compared to the deformation, but along the principal axes **n**:

$$\mathbf{V} = \sum_{i}^{2} \lambda_i \mathbf{n}_i \otimes \mathbf{n}_i, \tag{31}$$

where the dyadic product $\mathbf{n}_i \otimes \mathbf{n}_i$ changes the basis, by rotating the reference coordinate system to the directions of the principal axes **n**. Any second order tensor **T** can be rotated under a counter-clockwise angle to a different base with $\mathbf{T}' = \mathbf{Q}^T\mathbf{T}\mathbf{Q}$, using rotation matrix **Q** (eq. 13). Rotating back to the original frame occurs with $\mathbf{T} = \mathbf{Q}\mathbf{T}'\mathbf{Q}^T$. Thus, a more intuitive way of describing the stretch in terms of its eigenvalues is by changing the basis through a rotation of the coordinate system:

$$\mathbf{V} = \mathbf{Q}\boldsymbol{\Lambda}\mathbf{Q}^T \tag{32}$$

where $\boldsymbol{\Lambda} = \text{diag}(\lambda_1, \lambda_2)$. The principal stretches have a clear physical meaning, as Fig. 4 shows: the principal stretch vectors are the axes of the strain ellipse (e.g. Allmendinger *et al.* 2011). The principal strain magnitude can easily be expressed by subtracting 1 from λ_1, λ_2 (eq. 3). Orthogonal rotation matrix **Q** (eq. 13) rotates to the first principal axis $\mathbf{n}_1$ under an angle:

$$\Theta = \text{atan2}(n_1(2), n_1(1)). \tag{33}$$

2.5.4 Infinitesimal versus finite strain

Infinitesimal strain well describes small deformation, which can be understood as deformation where the shape of the deformed state **x** does not deviate significantly from the reference state **X**. We have briefly hinted at shortcomings of the infinitesimal strain tensor $\boldsymbol{\epsilon}$ in Section 2.5.1 and show here in more detail why many common quantities derived from infinitesimal strains are problematic for large deformations. Infinitesimal strains are especially unfit to describe large simple strains or rotations, because the approximation that strain and rotation can be summed no
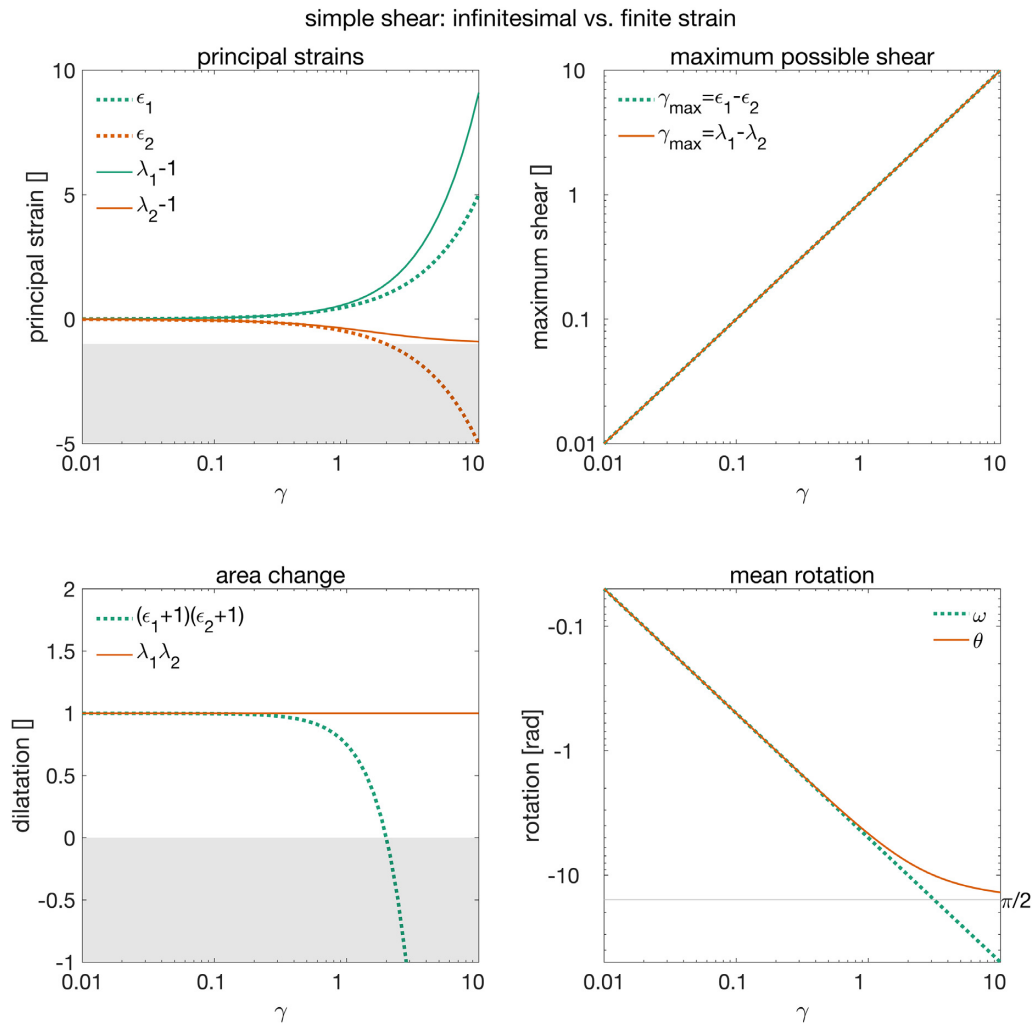
Figure 5. The limited validity of infinitesimal strain ϵ (eq. 15) to describe increasing deformation in the case of simple shear, with engineering strain γ, that is $\mathbf{F}_{ss} = \Gamma$ (eq. 21). Left-upper hand panel: principal strains, ϵ_1, ϵ_2 (infinitesimal) and λ_1, λ_2 (finite), where ϵ_1 does not capture the extension under large simple shears. Also, ϵ_2 linearly decreases with increasing γ, past the extensional strain limit of -1. The grey area depicts physically impossible values (Section 2.2). Right upper-hand panel: the maximum shear gives the same values for $\gamma_{max} = \epsilon_1 - \epsilon_2$ (infinitesimal) or $\gamma_{max} = \lambda_1 - \lambda_2$ (finite). Left lower-hand panel: area change in terms of dilatation (eq. 5). Dilatation using infinitesimal strains $dA/dA_0 = (\epsilon_1 + 1)(\epsilon_2 + 1)$ increasingly deviates for strains >0.1 from the exact values from $dA/dA_0 = \lambda_1 \lambda_2$. Moreover the infinitesimal strain can lead to physically impossible values when the dilatation drops below the minimum possible value of $dA/dA_0 = 0$ (grey area). Lower right-hand panel: mean rotation, using infinitesimal rotation ω (infinitesimal, eq. 17) or angle θ from the rotation matrix R (finite, eq. 28). Infinitesimal rotation is always proportional to γ for simple shear, while θ converges to $\pi/2$, which indicates the flattening of material under simple shear and the alignment of all material orientations with the *X*-axis.

longer holds. A comparison between the the strain tensor ϵ and stretch tensor $\mathbf{V}$ provides insight when the use of ϵ introduces significant errors to the interpretation of strain. Fig. 5 makes a comparison in terms of a number of scalar deformation measures: principal strains, maximum shear strain, dilatation and rotation.

As both ϵ and $\mathbf{V}$ are symmetric tensors, the Mohr circle applies to both, so that we can derive the maximum shear strain as a function of principal strains $\gamma_{max} = \epsilon_1 - \epsilon_2$, or principal stretches $\gamma_{max} = \lambda_1 - \lambda_2$.

Dilatation, area change, is the product of the principal stretches. In some studies the dilatation is represented by the divergence of the displacement field (Galland *et al.* 2016; Schellart *et al.* 2019) (i.e. $\epsilon_{xx} + \epsilon_{yy}$). This can be understood as an approximation to the true dilatation (eq. 5):

$$dA/dA_0 = \lambda_1 \lambda_2 = (1 + \epsilon_1)(1 + \epsilon_2) = 1 + \epsilon_1 + \epsilon_2 + \epsilon_1 \epsilon_2. \tag{34}$$

For small strains only, this reduces to:

$$dA/dA_0 \approx 1 + \epsilon_1 + \epsilon_2. \tag{35}$$

The last two terms are equal to the first invariant of the strain tensor:

$$\epsilon_1 + \epsilon_2 = \epsilon_{xx} + \epsilon_{yy} \tag{36}$$

The first invariant lacks the $\epsilon_1\epsilon_2$ term in eq. (34), which is why the divergence of the displacement field, or the first strain invariant, is not a good measure for area change in case of large deformation.

As an example we deform material under a simple shear γ, that is $\mathbf{F}_{ss} = \mathbf{\Gamma}$ (eq. 21). Fig. 5 demonstrates that for strains >0.1, principal strains, rotations and dilatation become increasingly unreliable when using ϵ instead of $\mathbf{V}$. For $\gamma > 2$ infinitesimal strains even provide physically impossible values for principal strains and dilatation (implying negative material vector lengths or negative area change). For maximum shear γ_{max}, both infinitesimal and finite tensors provide the same results. Infinitesimal rotation ω increases linearly with shear γ (to the extend of $>2\pi$ rotations), while θ correctly converges to $\pi/2$, which implies a gradual flattening of material under shear.

2.5.5 The shape change tensor of choice: V

To quantitatively describe shape changes, the left stretch tensor $\mathbf{V}$, expressed in its principal space (eq. 32), is thus most appropriate as it describes length changes as proportional stretches λ, which are directly related to the principal strains (eq 3). The length changes are provided in the final configuration, and being in the principal space these are independent from the arbitrary orientation of the chosen reference frame. The principal values of the finite strain tensors $\mathbf{E}$ and $\mathbf{E}^*$ are not proportional to length change, and are thus a less likely choice for the quantitative description of shape change. Infinitesimal strains ϵ are unfit for large stnorains in the case of rotations or simple shear. While the right-stretch tensor $\mathbf{U}$ is similar in many ways to $\mathbf{V}$, having the same principal stretch values, the direction of the principal axes are not in the final deformed state (see Fig. 4). The principal stretches from $\mathbf{V}$ have the advantage that these are directed in the stretch directions in the final, deformed configuration. In the following we will use the left stretch tensor $\mathbf{V}$ to discuss progressive deformation, after which we will develop qualitative measures of shape change in Section 2.7.

2.6 Incremental vs. finite strain for progressive deformation

We can write the final deformation $\mathbf{F}$ as a product of incremental deformations $\mathbf{F}^i$ (e.g. Ramberg 1975; Allmendinger *et al.* 2011)

$$\mathbf{F} = \mathbf{F}^n...\mathbf{F}^2\mathbf{F}^1. \tag{37}$$

Because:

$$d\mathbf{x}^1 = \mathbf{F}^1 d\mathbf{X}$$
$$d\mathbf{x}^2 = \mathbf{F}^2 d\mathbf{x}^1 = \mathbf{F}^2\mathbf{F}^1 d\mathbf{X}$$
$$d\mathbf{x}^n = \mathbf{F}d\mathbf{X} = \mathbf{F}^n...\mathbf{F}^2\mathbf{F}^1 d\mathbf{X}$$

Even though we can write the final deformation as a product of all previous incremental deformations, the final deformation is still insensitive to the deformation path, as this information is lost in the product of eq. (37).

Example: Differences between incremental and cumulative shear strains

Incremental and finite stretches may diverge in terms of the ratio between principal stretches during progressing deformation. This is especially the case for simple shear, but applies to any deformation that contains a shear component. During progressive simple shear ($a = 1, b = 1, \gamma \neq 0, \theta = 0$) the incremental deformation gradient takes the form $\mathbf{F}^i = \mathbf{\Gamma}$. Considering a constant incremental deformation gradient, the final simple shear deformation gradient $\mathbf{F}_{(ss)}$ after n increments becomes:

$$\mathbf{F}_{(ss)} = \begin{bmatrix} 1 & \gamma \\ 0 & 1 \end{bmatrix}^n = \begin{bmatrix} 1 & n\gamma \\ 0 & 1 \end{bmatrix}. \tag{38}$$

The principal stretches λ, of both $\mathbf{U}$ and $\mathbf{V}$, provide us with a description of the stretch that is independent from the coordinate orientation, and can be derived from the principal values μ of $\mathbf{C}$ (Malvern 1969), being solutions of the characteristic equation $|\mathbf{C} - \mu\mathbf{I}| = (C_{11} - \mu)(C_{22} - \mu) - C_{12}C_{21} = 0$. The left Cauchy–Green tensor for simple shear is:

$$\mathbf{C}_{(ss)} = \mathbf{F}_{(ss)}^T\mathbf{F}_{(ss)} = \begin{bmatrix} 1 & n\gamma \\ n\gamma & (n\gamma)^2 + 1 \end{bmatrix}. \tag{39}$$

The principal stretches λ follow from solving the characteristic equation, using the definition of $\mathbf{C}_{(ss)}$:

$$\lambda_{1(ss)} = \sqrt{\mu_{1(ss)}} = \sqrt{\frac{2 + (n\gamma)^2 + |n\gamma|\sqrt{4 + (n\gamma)^2}}{2}}$$

$$\lambda_{2(ss)} = \sqrt{\mu_{2(ss)}} = \sqrt{\frac{2 + (n\gamma)^2 - |n\gamma|\sqrt{4 + (n\gamma)^2}}{2}}.$$

Here λ_1 is the largest principal stretch. For small deformation $(\lambda_1 - 1) \approx -(\lambda_2 - 1)$, i.e. $\epsilon_1 \approx -\epsilon_2$, but for increasing n ϵ_1 will exceed ϵ_2 in magnitude (see Fig. 7). Notably, the direction of the largest principal stretch of $\mathbf{V}$, which provides the stretch in the deformed configuration, starts at $45°$ for small shears (and thus incremental simple shear) and converges slowly to $0°$ for large strains (Allmendinger *et al.* 2011), showing the gradual flattening of material and stretching in the direction of the X-axis.

The dilatation A/A_0 for progressive simple shear is (eq. 5):

$$A/A_0 = \lambda_{1(ss)}\lambda_{2(ss)} = \frac{1}{2}\sqrt{\left(2+(n\gamma)^2\right)^2 - (n\gamma)^2(4+(n\gamma)^2)} = \frac{1}{2}\sqrt{(n\gamma)^4 + 4(n\gamma)^2 + 4 - 4(n\gamma)^2 - (n\gamma)^4} = 1. \tag{40}$$

Which confirms that simple shear is area preserving (isochoric), and that:

$$\lambda_{2(ss)} = 1/\lambda_{1(ss)}. \tag{41}$$

This shows that for simple shear the relative magnitude of the two principal stretches (or principal strains) is different for small or large deformation.

2.7 Classifying strain type from continuum mechanics

Continuous vs. discrete deformation

Different types of incremental tectonic deformation lead to very distinct structures or fault patterns. Therefore, it is valuable to investigate the type of incremental deformation that has led to the current, finite, deformed state. In our framework we observe all deformation as distributed, because PIV averages deformation within a certain spatial window. Hence, up to this point, we have described deformation in a continuum approach. For our application, deformation in crustal tectonics, deformation is dominantly localized along narrow shear zones, or faults, and we aim to interpret continuous deformation as localized deformation. Especially, if a large fraction of the deformation is localized along discrete faults, we would like to classify the deformation as due to slip on normal, strike-slip, or thrust faults. While faulting incorporates shearing (simple shear) in three dimensions, in the semi-planar 2-D projection that we use, any deformation where the shear is in a vertical direction, the planar projected deformation becomes essentially a stretch.

Fault or shear zone types

Our aim is to classify three end-member fault (discrete fracture or narrow shear zone) types based on the continuum mechanics description: normal faulting, strike-slip and reverse/thrust faulting. While the end-member faults all involve shear, only strike-slip has a horizontal shear component. The continuum description of strike-slip in the horizontal plane is simple shear (as in Fig. 3). Normal faulting will lead to extension (stretch >1) of the horizontal plane surrounding the fault, in a direction perpendicular to the fault. On the other hand, reverse faulting (or thrusting) will lead to shortening (stretch <1) of the area surrounding the fault, with shortening in the direction perpendicular to the fault. For progressive deformation at reverse faults, footwall material that was first at the surface will be buried by the hanging wall material and, therefore, no longer be at the surface. Subsequently, that material will no longer be visible with PIV, resulting in an accumulation of virtual material points at the fault trace.

We furthermore consider two types of intermediate oblique faults: transtension, where faults experience strike-slip (simple shear) and fault-perpendicular extension (normal faulting), and transpression, as combination of strike-slip and fault-perpendicular shortening (reverse/thrust faults, Sanderson & Marchini 1984). We do not consider simple shear parallel stretching (Tikoff & Fossen 1999), which would lead to stretching of the actual faults, and which may be more applicable to ductile shear zones rather than faults (Means 1989). Stretching along one side of the fault only (e.g. Rutter *et al.* 2012) cannot be captured by the deformation gradient properly (as it concerns a non-homogeneous deformation). If the displacement field is however of sufficient resolution to capture the fault and stretching domain separately, the deformation can be adequately be described without fault-parallel deformation. In the following, we apply the same strain types to distributed deformation as well.

Strain type: small deformation

For small, infinitesimal strains one can classify the type of strain by comparing the magnitudes and signs of the largest and smallest principal infinitesimal strain, and the same holds for strain rates. Kreemer *et al.* (2014) defined a strain rate type measure $(\dot\epsilon_1 + \dot\epsilon_2)/max(|\dot\epsilon_1|, |\dot\epsilon_2|)$. For strike-slip both principal strain rates are similar in magnitude but different in sign, leading to a strain type value of close or equal to 0. For extension and shortening one principal strain rate is dominant and its value will be positive or negative, leading to strain type values of 1 for extension (>1 for extension in two directions), and -1 for shortening (<-1 for shortening in two directions).

Thus, based on the relative magnitude and signs of the largest and smallest magnitude principal strains ($|\epsilon_{max}| > |\epsilon_{min}|$) we can discriminate between strain type end-members:

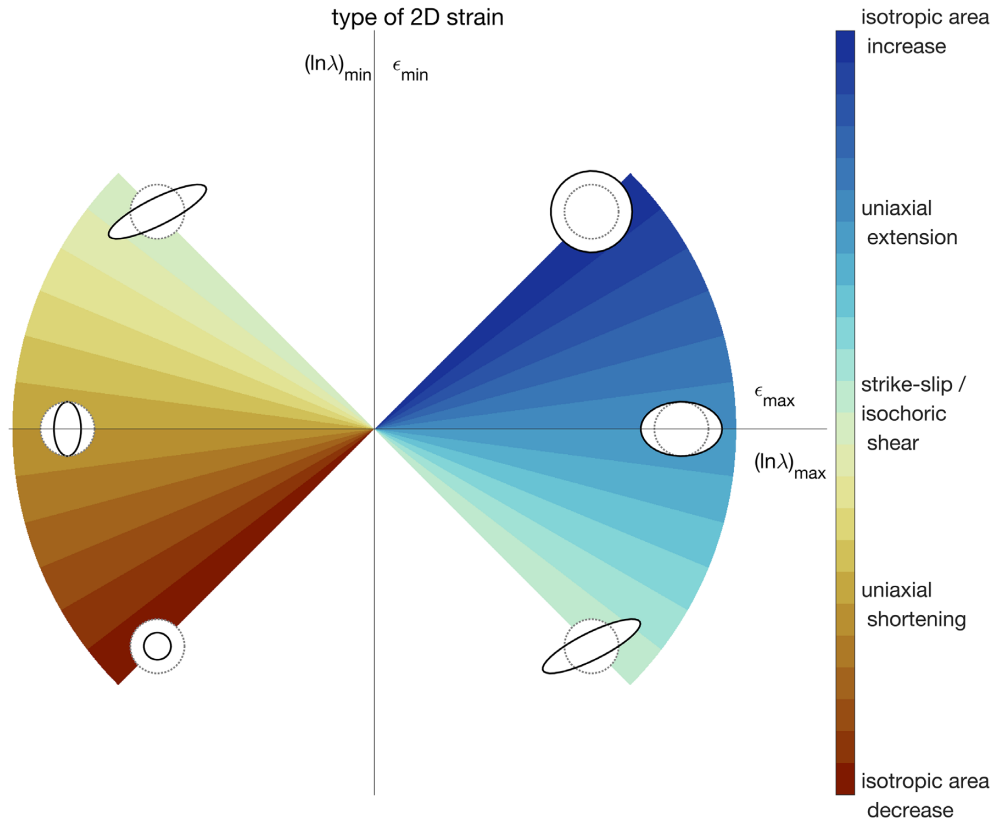(i) isotropic area increase: $\epsilon_{max} = \epsilon_{min}$ and $\epsilon_{max} > 0$ and $\epsilon_{min} > 0$

Figure 6. Strain type Φ as a function (eq. 43) of the angle ϕ between largest and smallest principal infinitesimal strains ($|\epsilon_{max}| > |\epsilon_{min}|$) (eq. 42) or logarithmic finite stretches ($|\ln \lambda|_{max} > |\ln \lambda|_{min}$) (eq. 47). Based on the relation between the two principal values in the horizontal plane, in terms of magnitude and sign, we can define a range of types of strain end-members: (a) isotropic area increase: $\epsilon_{max} = \epsilon_{min}$ and $\epsilon_{max} > 0$ and $\epsilon_{min} > 0$, (b) uniaxial extension: $\epsilon_{max} > 0$ and $\epsilon_{min} = 0$, (c) strike-slip (simple shear): $|\epsilon_{max}| = |\epsilon_{min}|$ and $\epsilon_{max} > 0$ and sign(ϵ_{max}) = $-$sign(ϵ_{min}), (d) uniaxial shortening: $\epsilon_{max} < 0$ and $\epsilon_{min} = 0$ (e) isotropic area decrease: $\epsilon_{max} = \epsilon_{min}$ and $\epsilon_{max} < 0$ and $\epsilon_{min} < 0$ The strain type Φ is a continuous scale, and within a tectonic context we can expect intermediate, oblique, strain types, notably transtension as an intermediate case between strike-slip and extension; and transpression as an intermediate between strike-slip and shortening. All isochoric (area preserving) shears have the same strain type Φ as strike-slip/simple shear, we discuss implications in Section 6.3.

(ii) uniaxial extension: $\epsilon_{max} > 0$ and $\epsilon_{min} = 0$

(iii) strike-slip (simple shear): $|\epsilon_{max}| = |\epsilon_{min}|$ and $\epsilon_{max} > 0$ and sign(ϵ_{max}) = $-$sign(ϵ_{min})

(iv) uniaxial shortening: $\epsilon_{max} < 0$ and $\epsilon_{min} = 0$

(v) isotropic area decrease: $\epsilon_{max} = \epsilon_{min}$ and $\epsilon_{max} < 0$ and $\epsilon_{min} < 0$

We adjust the Kreemer *et al.* (2014) model, initially for small deformation, and we further extend the model to large deformation in Section 2.7, where we also discuss intermediate strain types. We define a Cartesian coordinate system, shown in Fig. 6, where the *x*-axis represents the largest magnitude principal strain and the *y*-axis represents the smallest magnitude principal strain. To define a strain type measure, we determine the (counter-clockwise) angle ϕ measured from the ϵ_{max}-axis in the ϵ_{max}, ϵ_{min} space:

$$\phi = \text{atan2}(\epsilon_{min}, \epsilon_{max}). \tag{42}$$

Here ϵ_{max} and ϵ_{min} represent the principal strain values with the largest and smallest absolute values. The angle ϕ thus provides the counter-clockwise angle between the two principal values, measured from the ϵ_{max} axis. Fig. 6 gives a visual interpretation of angle ϕ, as a function of the two principal strains (eq. 42). Angle ϕ being a discontinuous function, we convert ϕ into a continuous strain type measure Φ by:

$$\Phi = \begin{cases} -\phi - \frac{5}{8}\pi & \text{if } \phi \le -\frac{3}{4}\pi \\ \phi + \frac{1}{4}\pi & \text{if } -\frac{1}{4}\pi \le \phi \le \frac{1}{4}\pi \\ -\phi + \frac{3}{4}\pi & \text{if } \phi \ge \frac{3}{4}\pi \end{cases}. \tag{43}$$

Φ thus becomes centered around strike-slip ($\Phi = 0$) and has a range $[-\frac{\pi}{2}, \frac{\pi}{2}]$, of which the limits correspond to isotropic area decrease and isotropic area increase, respectively. At a later stage we will discuss how pure shear (irrotational shear), and oblique faults fit in the strain type.
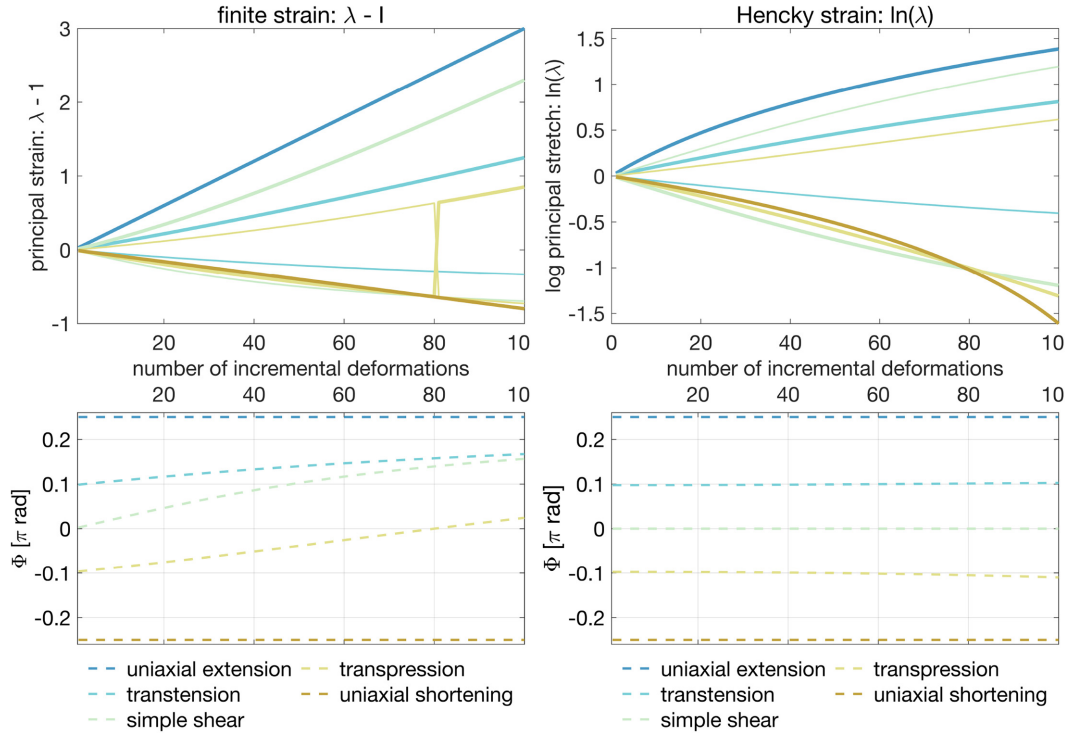
Figure 7. Principal strains for progressive strain with constant incremental displacement gradients, for the cases (a) uniaxial extension ($\mathbf{F}^i$: $a = 1 + 3 \times 10^{-2}$, $b = 1$, $\gamma = 0$) (b) transtension ($\mathbf{F}^i$: $a = 1$, $b = 1 + 5 \times 10^{-3}$, $\gamma = 1.5 \times 10^{-2}$) (c) strike-slip ($\mathbf{F}^i$: $a = 1$, $b = 1$, $\gamma = 3 \times 10^{-2}$) (d) transpression ($\mathbf{F}^i$: $a = 1$, $b = 1 - 5 \times 10^{-3}$, $\gamma = 1.5 \times 10^{-2}$) (e) uni-axial extension ($\mathbf{F}^i$: $a = 1 - 8 \times 10^{-3}$, $b = 1$, $\gamma = 0$) Left-hand panel: principal finite strains max($|\lambda - 1|$) and min($|\lambda - 1|$) (thinner lines, only displayed if non-zero) and the strain type angle Φ based on finite strain (dashed lines). Here it is clear that Φ is not constant for progressing strain for deformation including shear. The principal stretches can thus not be used to define a strain type for large deformation. Note: there is a reversal for transpression of which principal stretch has the largest magnitude. Right-hand panel: logarithm of the principal strains $ln\boldsymbol{\lambda}$. Here it shows that Φ is constant with increasing deformation for strike-slip, extension and shortening; for transtension and transpression it is nearly constant. Colours correspond to the infinitesimal strains from Fig. 6.

Strain type: large deformation

We now consider progressive deformation, leading to large, finite deformation. In considering the evolution of principal strains for progressive, steady deformation, we assume a constant displacement gradient $\frac{\partial \mathbf{u}}{\partial \mathbf{X}}$. This leads to a deformation gradient as function of number of increments n:

$$\mathbf{F}(n) = \left(\frac{\partial \mathbf{u}}{\partial \mathbf{X}}\right)^i n + \mathbf{I} = \left(\mathbf{F}^i - \mathbf{I}\right)n + \mathbf{I}. \tag{44}$$

Fig. 7 shows the principal strain ($\lambda - 1$) evolution for a constant incremental displacement gradient, for the cases extension, shortening, strike-slip and oblique combinations of extension and strike-slip: transtension; and shortening and strike-slip: transpression. We construct incremental deformation gradients $\mathbf{F}^i$ using a rigid body rotation matrix $\mathbf{Q}$, distortion matrices $\boldsymbol{\Lambda}$ (extension and shortening), $\boldsymbol{\Gamma}$ (strike-slip) or the product $\boldsymbol{\Lambda}\boldsymbol{\Gamma}$ (transtension and transpression). As we work with principal values, which are insensitive to rotation, we do not specify a rotation angle in the following. We define simple shear γ along the X-axis, and extensional components along the Y-axis (e.g. perpendicular to the simple shear direction: $b \neq 1$; $a = 1$), see eq. (12).

From the left panel of Fig. 7, it is clear that for all cases that contain shearing, the largest principal strain $\lambda_{\max} - 1$ will increasingly become dominant for progressing strain. Thus, the angle Φ (dashed lines) is not constant with increasing strain. Therefore we cannot use finite strain to define a strain type in a similar way as for small deformation (eq. 42), as large shear and extension will have a seemingly similar dominance of the largest principal stretch or strain.

From eq. (41) we know that the principal stretches for simple shear/strike-slip relate as $\lambda_{2(ss)} = 1/\lambda_{1(ss)}$, which implies that:

$$ln\lambda_{2(ss)} = -ln\lambda_{1(ss)} \tag{45}$$

Therefore, for strike-slip we can also make use of the logarithm of the stretch, and obtain a constant angle ϕ, irrespective of the magnitude of the finite stretch. This logarithmic stretch is related to Hencky strain, which from the viewpoint of the deformed configuration, is defined as (Xiao *et al.* 1997):

$$ln\mathbf{V} = \sum_{i=1}^{2} (ln\lambda_i)\mathbf{n}_i \otimes \mathbf{n}_i \tag{46}$$

with principal stretches λ_i and the respective eigenvectors $\mathbf{n}_i$ of $\mathbf{V}$, see also eq. (31).

In case of uniaxial extension or shortening, the finite stretch for a constant displacement gradient, or a constant incremental strain, has always one principal stretch equal to one, and thus one zero principal strain. For uniaxial extension or shortening the angle Φ is thus constant, irrespective of the magnitude of deformation. Trivially, the logarithmic principal stretch leads to the same constant Φ. The right-hand panel of Fig. 7 shows that for a constant incremental displacement gradient and Hencky strains, our strain type measure is constant for strike-slip, as well as extension and shortening. For oblique deformation we obtain a strain type based on the logarithmic Hencky strains that is nearly constant with increasing strain. The change in Φ for oblique deformation is sufficiently small to be able to use the measure for qualitative classification of the strain type. Because the strain type is constant for a certain type of deformation, irrespective of its size, the temporal behaviour of deformation is not of importance for the strain classification. We can thus use the Hencky principal strains to classify the type of strain, in a similar way as for small, incremental strains:

$$\phi = \text{atan2}(\ln\lambda(i_{\min}), \ln\lambda(i_{\max})). \tag{47}$$

Here, $i_{\min}$ and $i_{\max}$ are the indices of the absolute minimum and absolute maximum principal stretch λ, such that $|\ln\lambda(i_{\max})| > |\ln\lambda(i_{\min})|$. The continuous strain type Φ follows from ϕ using eq. (43).

In terms of Hencky strains, our definition for strike-slip covers both simple shear (rotational) as well as pure shear (irrotational) or combinations of both, sub-simple shear, as these lead to $\ln\lambda_2 = -\ln\lambda_1$. On the other hand, it can be expected that for brittle deformation, pure shear is partitioned along (oblique) strike-slip, thrust and extensional faults (e.g. Fossen 2016), see Section 6.3 for a discussion.

Another advantage of Hencky strains for large deformation is that $ln\lambda$ spans a range between $[-\infty, \infty]$ instead of $[0, \infty]$. The Hencky principal strains thus have a more symmetric distribution around 0 (no deformation) compared to λ, where shortening falls in the $[0, 1]$ range.

We expect that in a tectonic context, isotropic area changes will not occur at shear zone scales. For faulting, extension, strike-slip and shortening can be regarded as end-member models (Fossen *et al.* 1994). Localized isotropic deformation requires stretching in two orthogonal directions, which cannot be accomplished with slip on faults. For more distributed deformation we expect that isotropic area increase may occur, for example deformation due to gravitational collapse at topographic gradients (see Section 5.3). Isotropic deformation combined with shear can not be discriminated from two orthogonal stretches with different magnitude, but the same sign.

3 APPLICATION: STRAIN TYPE FOR ROTATING ELEMENTS UNDER DIFFERENT TYPES OF DEFORMATION

As a first test, we apply our strain type classification to individual square elements that we deform using a constant incremental deformation gradient $\mathbf{F}^i$, ranging from shortening, via transpression to strike-slip, and subsequently via transtension to extension. We also apply variable rotation to illustrate the independence of the strain type on rigid body rotations.

Fig. 8 shows the principal stretches and direction of $\mathbf{V}$ (left-hand panel) and strain types (right-hand panel) for the final configuration. The first 7 rows show a gradual change from shortening (left) to strike-slip to extension. The 2 last columns contain pure shear and no shape change. The rows apply varying rotation, with the middle row no rotation, the upper rows clockwise rotation and the lower rows counter-clockwise rotation. Mathematically, the progressive deformation $\mathbf{F}(n)$ at epoch n is defined as:

$$\mathbf{F}(n) = \mathbf{Q}\tilde{\mathbf{F}} = \begin{bmatrix} cos(\theta n) & -sin(\theta n) \\ sin(\theta n) & cos(\theta n) \end{bmatrix} \begin{bmatrix} a & a\gamma \\ 0 & b \end{bmatrix}^n \tag{48}$$

The strain types in Fig. 8 are consistent with the applied deformation gradient, with gradual transitions between shortening through strike-slip to extension. Rotation has, as expected, no effect on the derived strain characterization.

4 APPLICATION: SYNTHETIC ROTATING SHEAR ZONE

In the following test we define a shear zone (simple shear) that we rotate at the same time, to check whether our methods consistently determine the deformation as strike-slip. We define the shear zone by defining Eulerian displacements δu on fixed, regularly spaced points. First, we define strike-slip displacements d in the local, shear zone corotating frame, which are defined at epoch i as: $\mathbf{x}'(i) = \mathbf{Q}(\theta^i)\mathbf{x}$. Rotation matrix $\mathbf{Q}$ (eq. 13) is a function of angle $\theta^i = 60\frac{i}{n}$.

$$d = \frac{\Delta u}{n}\text{erf}(x'(i)b) \tag{49}$$

Here Δu is the final displacement after n epochs, erf the error function, x the coordinate perpendicular to the shear zone, with a range centered around 0, and b is a parameter to scale the width of the shear zone. The displacement vector then becomes:

$$\begin{bmatrix} \delta u_x \\ \delta u_y \end{bmatrix} = \mathbf{Q}\begin{bmatrix} 0 \\ d \end{bmatrix} + \mathbf{Q}\begin{bmatrix} x \\ y \end{bmatrix} - \begin{bmatrix} x \\ y \end{bmatrix}, \tag{50}$$

where the first term represents the rotated shear displacements, and the last two terms combined are the rotation contribution. Fig. 9 shows the
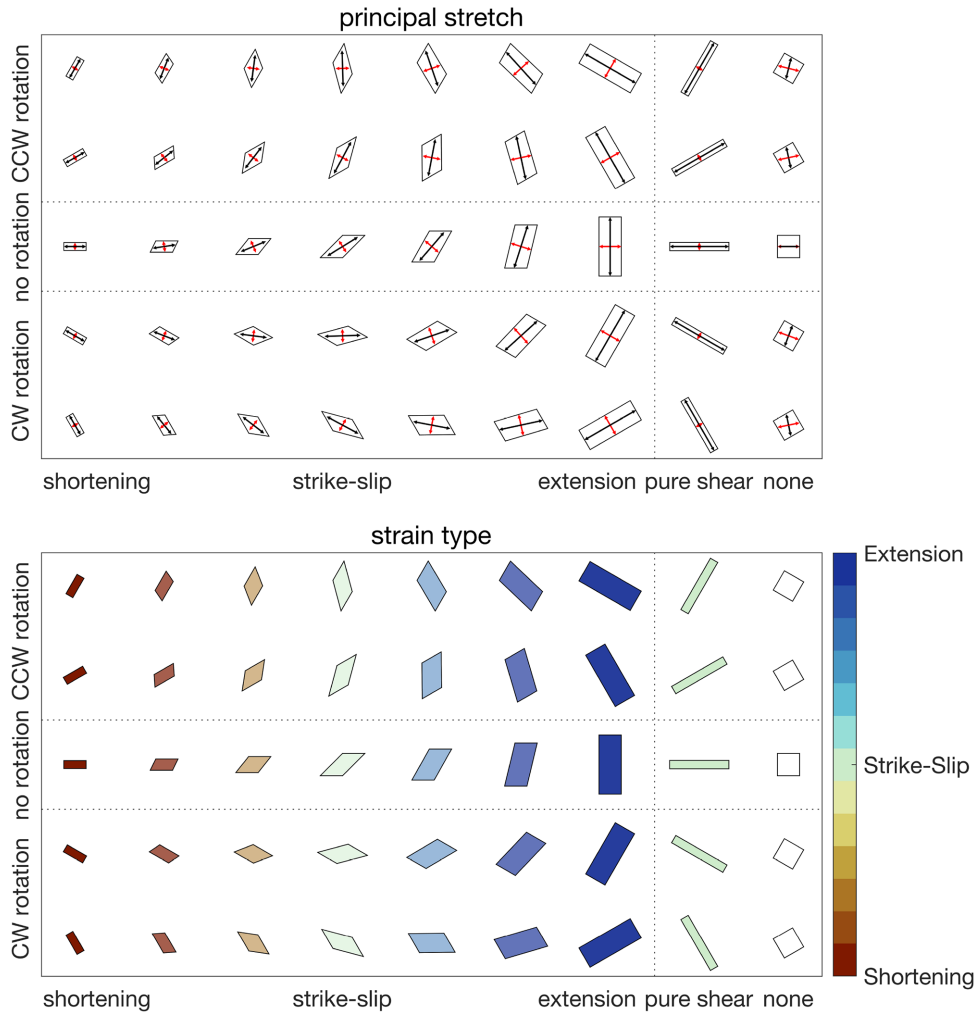
Figure 8. Synthetic test using individual elements that are deformed using a constant incremental distortion tensor $\tilde{\mathbf{F}}$ (eq. 48), shown after 20 steps. In the *x*-direction we vary the distortion parameters, in the *y*-direction we vary the amount of rotation. Left-hand panel: principal stretches $\boldsymbol{\lambda}$ from left-stretch tensor $\mathbf{V}$, with the largest principal stretch in black, and the smallest in red. Right-hand panel: strain type Φ based on the logarithmic principal Hencky strains $ln\boldsymbol{\lambda}$ (eq. 46). Distortion parameters used for the first seven columns, from left to right: $a = 1$, $b = 1 + [-1, -2/3, -1/3, 0, 1/3, 2/3, 1] \cdot 5 \times 10^{-2}$ and $\gamma = [0, 1/3, 2/3, 1, 2/3, 1/3, 1] \cdot 5 \times 10^{-2}$. The 8th column with pure shear has $a = 1 + 5 \times 10^{-2}$ and $b = 1/a$, $\gamma = 0$. The last column has $a = 1$, $b = 1$, $\gamma = 0$. Rotation angle θ varies linearly between the rows between the values $[\frac{2}{3}\pi, -\frac{2}{3}\pi]$.
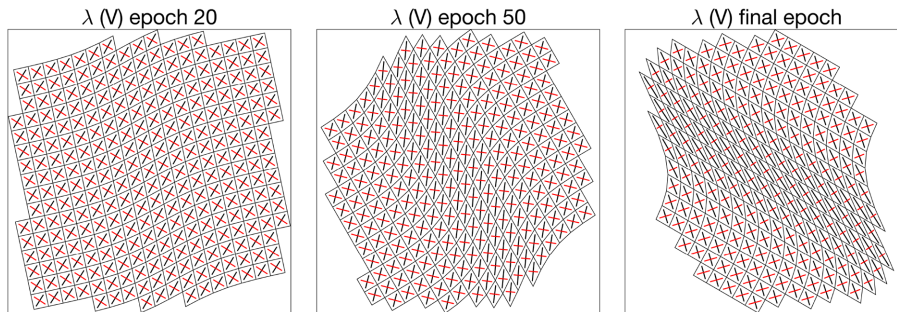

Figure 9. Synthetic test, representing a counter-clockwise rotating shear zone, with results for three epochs: 20, 50 and 100 (final). Principal stretches $\boldsymbol{\lambda}$ of left-stretch $\mathbf{V}$ tensor, with largest λ in black, the smallest in red. As some elements move outside the region for which we describe the Eulerian displacements, we loose part of the model during deformation evolution.
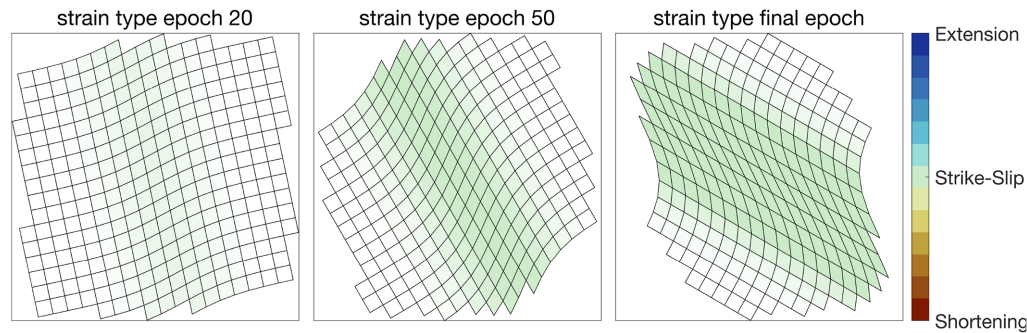
Figure 10. Synthetic test, representing a counter-clockwise rotating shear zone, with results for 3 epochs: 20, 50 and 100 (final). Strain type Φ based on Hencky principal strains $ln\lambda$, eq. (47). Elements with Hencky principal strain magnitudes below the 50 percentile, we render increasingly transparant.
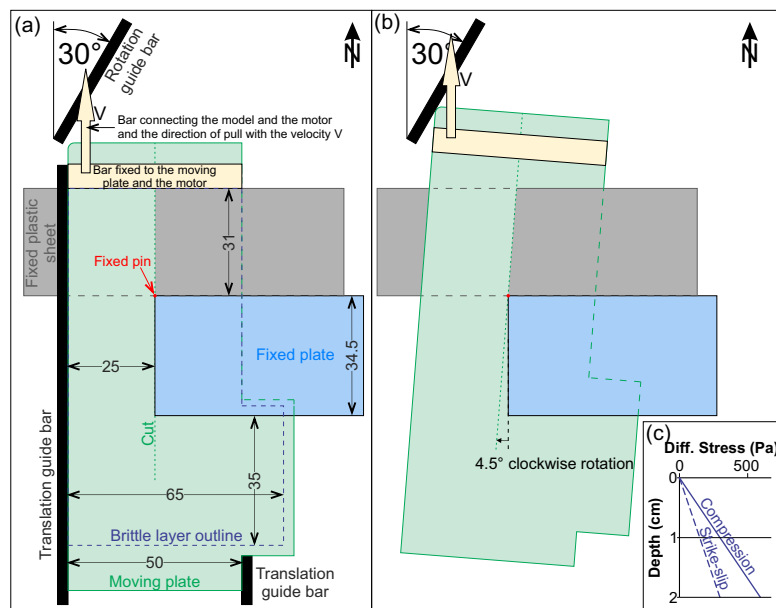

Figure 11. Model set-up: (a) Initial model set-up. All numbers are in centimeters. (b) Model configuration at the end of the experiment. Moving plate kinematics include the first step of 4 cm of translation and the second step of combined translation/rotation resulting in total of 9 cm of northward translation and 4.5° clockwise rotation. (c) Strength profile for the model. Note that the orientation in model is geographical, with up being relative North.

evolution of the principal stretches and principal directions of **V**, also showing the increasing dominance of λ_1 for progressive deformation. Fig. 10 shows the consistently constant strike-slip strain type Φ for the full model and time span, unaffected by rigid body rotations.

5 APPLICATION: ANALOGUE MODEL

In a final step, we analyse incremental displacements derived from successive images of an analogue, laboratory model of a coupled convergent and strike-slip tectonic setting. We have designed a model setup such that different regions of the model experience a wide range of different types of deformation: strike-slip faults (simple shear), normal faulting (extension) and thrust faulting (shortening). In the later stages of the model evolution, a part of the model undergoes a clockwise rigid body rotation, which allows for testing of the strain type analysis to rotations. A north–south horizontal velocity discontinuity in the middle of the model leads to a strike-slip zone, and a fixed indenter is responsible for thrusting in the southern model domain in front of the indenter, see Fig. 11. Due to the evolution of topography in front of the indenter, we expect to see normal faulting or distributed extension as well, due to gravitational collapse at topographic gradients. The experimental set-up is relevant for many natural indentation settings, for example India or Arabia indentation into Eurasia (Tapponnier *et al.* 1982; Hubert-Ferrari *et al.* 2003) or the lateral extrusion of the Alps (Ratschbacher *et al.* 1991), where shortening in front of an indenter is transferred around the corner into strike-slip deformation along the lateral indenter margin. Our experimental setup merely serves as the proof of concept for our strain analysis; further developed experiments are part of Krstekanić *et al.* that compares modeling results to natural cases of curved strike-slip systems at the lateral ends of a rigid indenter.

5.1 Analogue model experimental set-up

The laboratory model consists of a single 2 cm thick brittle layer made of dry quartz sand, sieved to grain sizes of 100–300 μm, with density of $\rho = 1.500 \, \text{kg m}^{-3}$, a coefficient of peak friction $\mu_P = 0.63$ and cohesion of 10–40 Pa (Willingshofer *et al.* 2018). The length ratio $L^* = L_{\text{model}}/L_{\text{nature}} = 1.5 \times 10^{-6}$, which means that total thickness of 2.0 cm of our model scales to 13.3 km in nature. The strength profile as a function of depth (inset of Fig. 11) follows the equations by (Brun 2002), where the strength profile represents the initial conditions.

Fig. 11 shows how we apply a horizontal velocity discontinuity to the quartz sand layer by one mobile and two fixed plastic plates/sheets. For the description of the model we adopt a geographical coordinate system. The moving plate (green in Fig. 11) lies below the entire model and is connected to an electric motor that applies a northward pull at a constant velocity of $V = 10 \, \text{cm hr}^{-1}$. A narrow N–S cut in the middle of this plastic plate (dashed green line in Fig. 11) allows for the translation and rotation of the moving plate around a fixed pin (red dot in Fig. 11). This pin represents the pole of rotation and is fixed to the stable plate (blue in Fig. 11) at its northwestern corner. The third basal plastic sheet, located north of the blue plastic plate, is also fixed (grey in Fig. 11). Directly north of the blue plate, the grey sheet is placed on top of the moving plate, while in the northwestern part of the model it is located below the moving plate (Fig. 11), which is facilitated by the cut in the moving plate.

Our set-up allows the moving plate to translate into the area north of the pin, imposing a convergent deformation south of the stable region (i.e. blue plate in Fig. 11) as well as a clockwise rotation. With this configuration, velocity discontinuities are located at two locations: (i) at the bottom of the model along the southern and western margin of the stable blue plate and (ii) along the contact between moving plate and grey fixed sheet.

Applied displacements in the experiment fall in two distinct phases. In the first phase, the motor pull induces four cm of northward translation, while translation guide bars (left-hand panel of Fig. 11) prevent rotation. The second phase starts when the moving plate hits the rotation guide bar. At that moment, the translation guide bars are removed, enabling coupled rotational and translational movement of the moving plate (right-hand panel of Fig. 11). When depressions deeper than 1 mm form, we fill them manually with alternating layers of differently coloured sand, representing syn-kinematic sedimentation. We stop the experiment when the total clockwise rotation reaches 4.5° and the total northward offset along the western margin of the stationary blue plate is 9 cm (configuration as in right-hand panel of Fig. 11).

5.2 Tectonic structure analysis and PIV displacement analysis

The PIV analysis is based on top images of the full experiment, taken every 45 s. During this interval the N–S translation of the moving plate is 1.25 mm. For the analysis we focus on the central part of the experiment (blue outlines of Video S1), which in the images measures 3254 times 1501 pixels. We analyse this area of interest using the software PIVlab (Thielicke & Stamhuis 2014). We pre-process images using the PIVlab CLAHE filter and the auto contrast stretch to optimize the contrasts. For the PIV, the first pass uses an interrogation area of 88 px, and a 50 per cent overlap of the interrogation areas. In subsequent two passes, the interrogation areas are 64, 32 px, respectively. We post-process PIV-results by removing displacements that are larger than seven times the displacement standard deviation, and manually remove outliers. PIVlab interpolates the resulting missing data.

Furthermore, we visually analyse fault structures in the final configuration. Offsets between passive marker lines that are east-west oriented in the model indicate strike-slip faults. Normal and thrust faults result in topographic gradients, where normal faults have a visible scarp. Cross sections taken after the model finishes, combined with the top view images, provide information of the faults with localized slip. Video S1 contains a video of the model evolution. Images shown in Figs 12–15 have adjusted colour intensities for better contrast: we linearly scale the original image RGB colour intensities in the 0.15–99.85 percentiles to the [0 1] intensity range, as the original colours span only a limited part of the intensity range.

5.3 General model evolution

Initial deformation

Fig. 12 depicts the principal stretches λ_{max}, λ_{min} and our inferred strain type after 7.5 min of model evolution, next to the image at the same time. Principal stretches >1 imply extensional deformation and are generally shown by the largest principal stretch λ_{max}, while stretches <1 denote shortening deformation (eq. 31). The strain type Φ is based on the relative magnitudes of the logarithmic principal stretches (Hencky strains), see Section 2.7. At this point in the model evolution the initial deformation is distributed in broad shear zones: along the N–S velocity discontinuity with transtension bounded at two sides with transpression, rather than by pure strike-slip; indicated in Fig. 12 by (1). Gomes *et al.* (2019) attribute the deformation in the latter shear zone to dilation of the granular material above the velocity discontinuity. In front of the stable region, along the E–W oriented velocity discontinuity, two zones of shortening evolve. This early structural pattern consists of a top-to-N basal thrust (2) and one top-to-S backthrust (3).
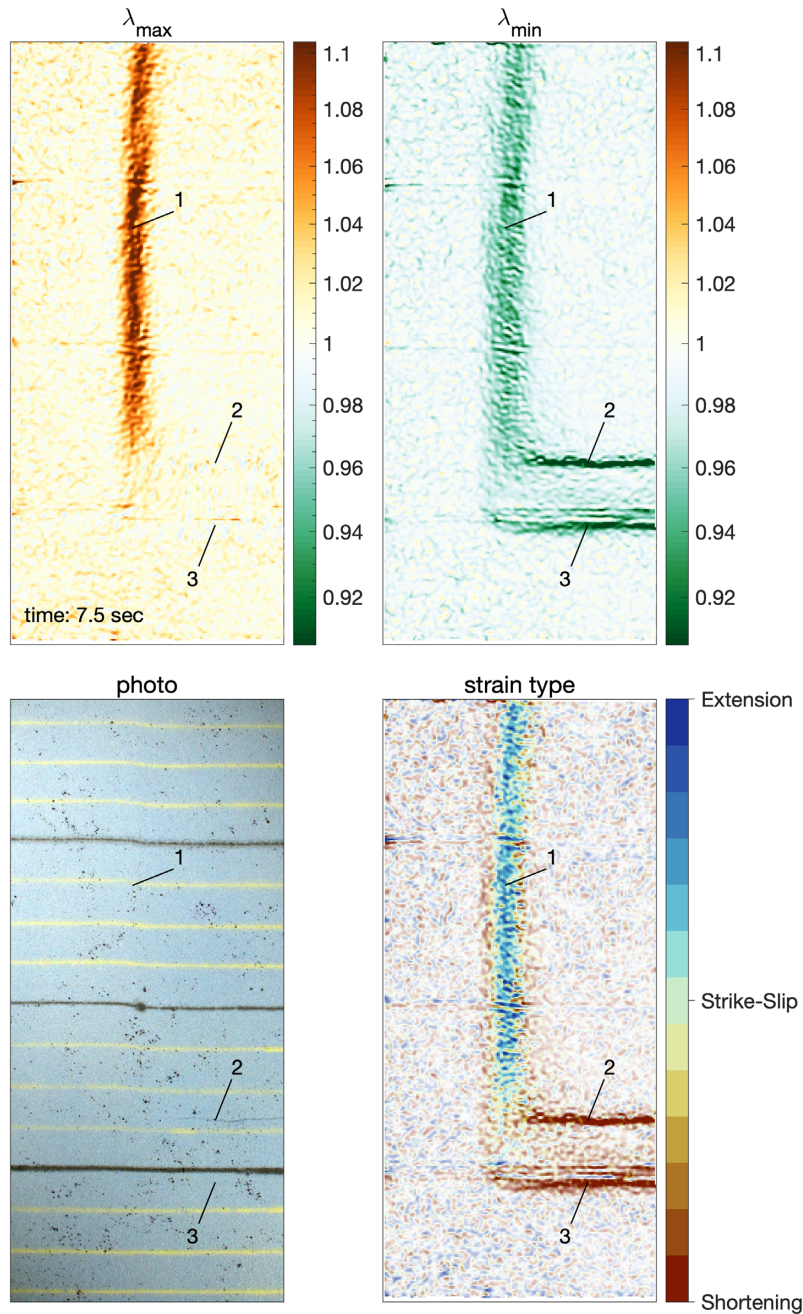
Figure 12. Principal stretches λ_{max}, λ_{min} ($\lambda = 1$ represents no length change) and strain type Φ at 7.5 min of model evolution: shortening (red), strike-slip (green) and extension (blue), with intermediate, oblique deformation at intermediate colours. Numbers indicate: (1) broad shear zone; (2) basal thrust and (3) backthrust.

Development of faults

At ≈ 1 cm of northward displacement of the moving plate (after 15 min), strain localizes into narrow zones of deformation, as Fig. 13 shows. Along the N–S oriented velocity discontinuity, this early deformation is accommodated by en-echelon NNE–SSW oriented Riedel R-shears (4). Principal stretches λ in Fig. 13 show NNW–SSE deformation features (5) (P-shear structures), which are characterized by lower strain than the R-shears. Inspection of the photos suggests that the strain levels in the connecting shear zones are too low to result in brittle failure, as no fault structures have formed here. At the same time, the basal thrust (2) and backthrust (3) become sharper features above the E–W striking boundary of the velocity discontinuity. Around the SW corner of the stable region, this distributed strike-slip deformation (6) connects and transfers into thrusting accommodated by the basal thrust and backthrust system in which new thrusts start to develop (7). Above the basal thrust, in its immediate hinterland, distributed extensional deformation takes place (8). This extension accommodates the transition between the ramp and the upper flat segments of the basal thrust. With the progress of northward translation, additional en-echelon R-shears form,
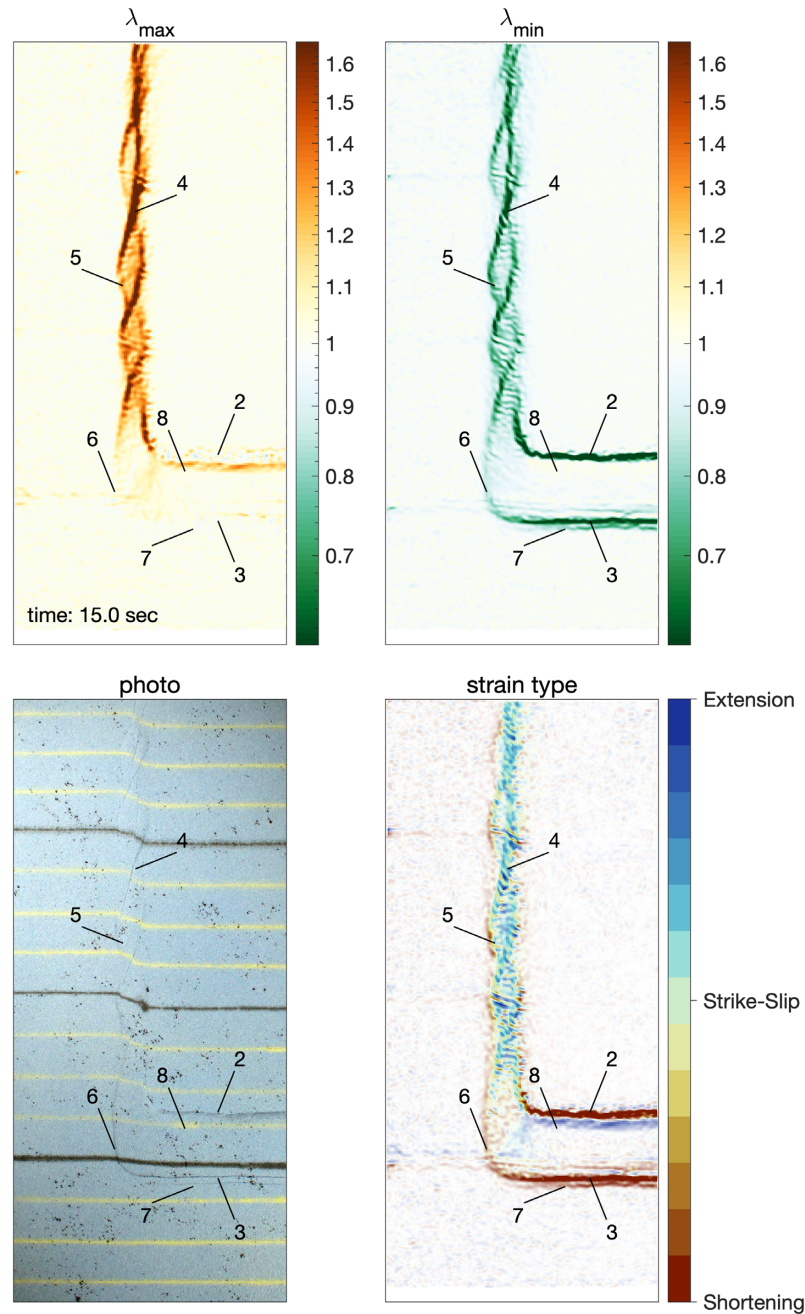
Figure 13. Principal stretches λ_{max}, λ_{min} ($\lambda = 1$ represents no length change) and strain type Φ at 15 min of model evolution: shortening (red), strike-slip (green) and extension (blue), with intermediate, oblique deformation at intermediate colours. Numbers indicate: (2) basal thrust; (3) first backthrust; (4) Riedel R-shear; (5) Riedel P-shear; (6) fault connecting basal-thrust and strike-slip zone; (7) new backthrust and (8) zone of extensional surface deformation.

visible in Fig. 13 as strain features with the same orientation as (4). The transpressional area at the sides of the shear zone, bounding the Riedel shears, becomes slightly elevated when positive flower structures form.

Merging of strike-slip faults and new backthrusts

By the end of the northward translation stage (4 cm of moving sheet displacement, at about 30 min), all R-shears have become connected to form a continuous strike-slip fault zone where the eastern fault (9) takes up most of the displacement, see Fig. 14. This process is also visible in the incremental rotation ω in video S2. The previous fault that connected the strike-slip zone to the backthrusts (6) is well visible in the cumulative deformation, but since the eastern strike-slip fault is now dominant (9), a new fault propagates toward the south (10) to connect with the newest formed backthrust and thus cuts through the previously formed thrust wedge. The latter fault is short-lived, so its effect on the cumulative deformation is small, but it is well visible in the top-view photo as well as in the incremental strain in video S2. To the SW
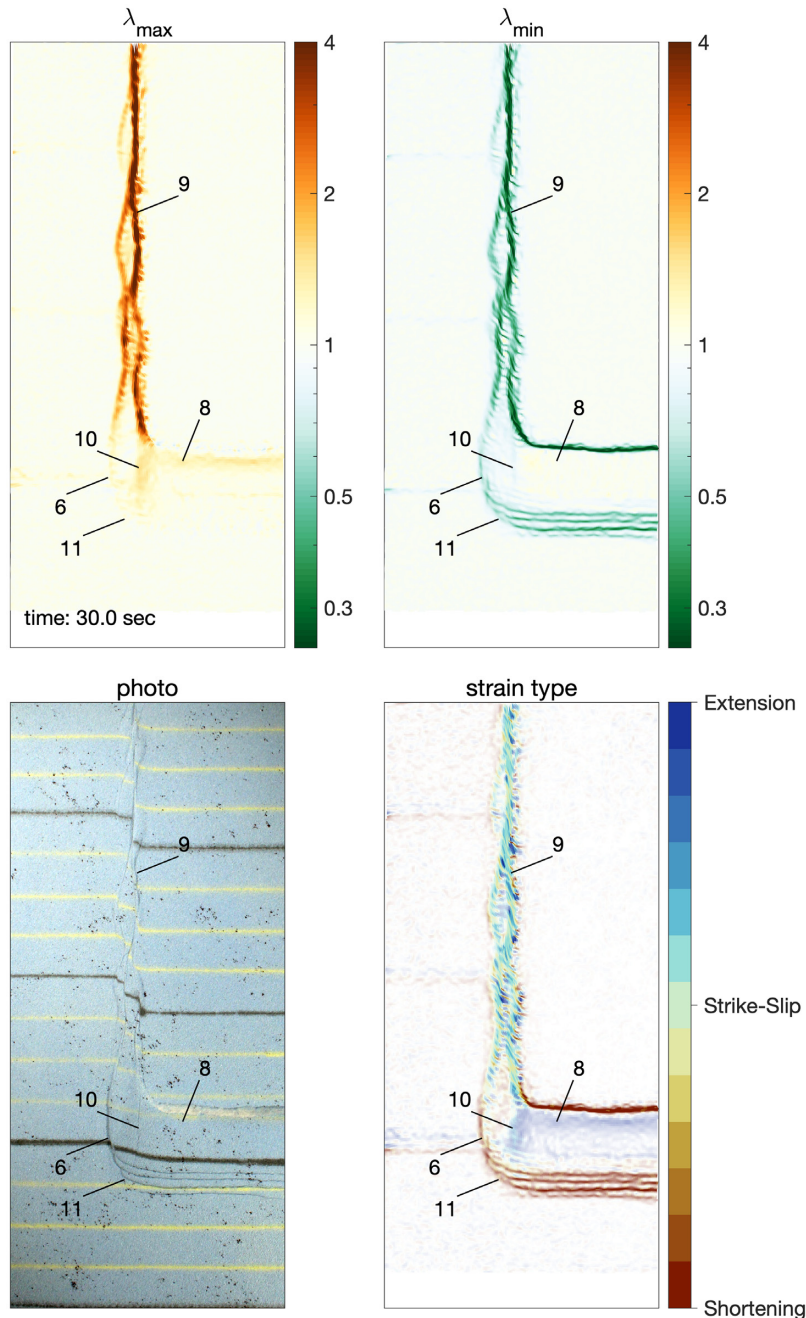
Figure 14. Principal stretches λ_{max}, λ_{min} ($\lambda = 1$ represents no length change) and strain type Φ at 30 min of model evolution: shortening (red), strike-slip (green) and extension (blue), with intermediate, oblique deformation at intermediate colours. Numbers indicate: (6) fault connecting basal-thrust and western strike-slip fault; (8) zone of extensional surface deformation; (9) dominant strike-slip fault; (10) strike-slip propagation through the wedge and (11) transpressional deformation on backthrust.

of the indenter, the backthrusts become progressively more transpressional (11), as shown by the orange colours in the strain type panel. The distributed extensional deformation on top of the wedge (8) now occurs in large areas above the basal thrust.

Effect of concurrent translation and rotation

After the onset of rotation (starting after 30 min) and until the end of the experiment (63.8 min), the structural pattern becomes more complex. Fig. 15 shows that in the north (i.e. north of the pole of rotation) a transpressional wedge forms, with oblique-slip thrusts (12) bounding the strike-slip deformation zone. In the N–S deformation zone we find the main strike-slip fault (9) that accommodates most of the deformation at the east of the shear zone. Fig. 16 clearly shows this combination of strike-slip and thrusting in cross-section a–a'. To the south of the
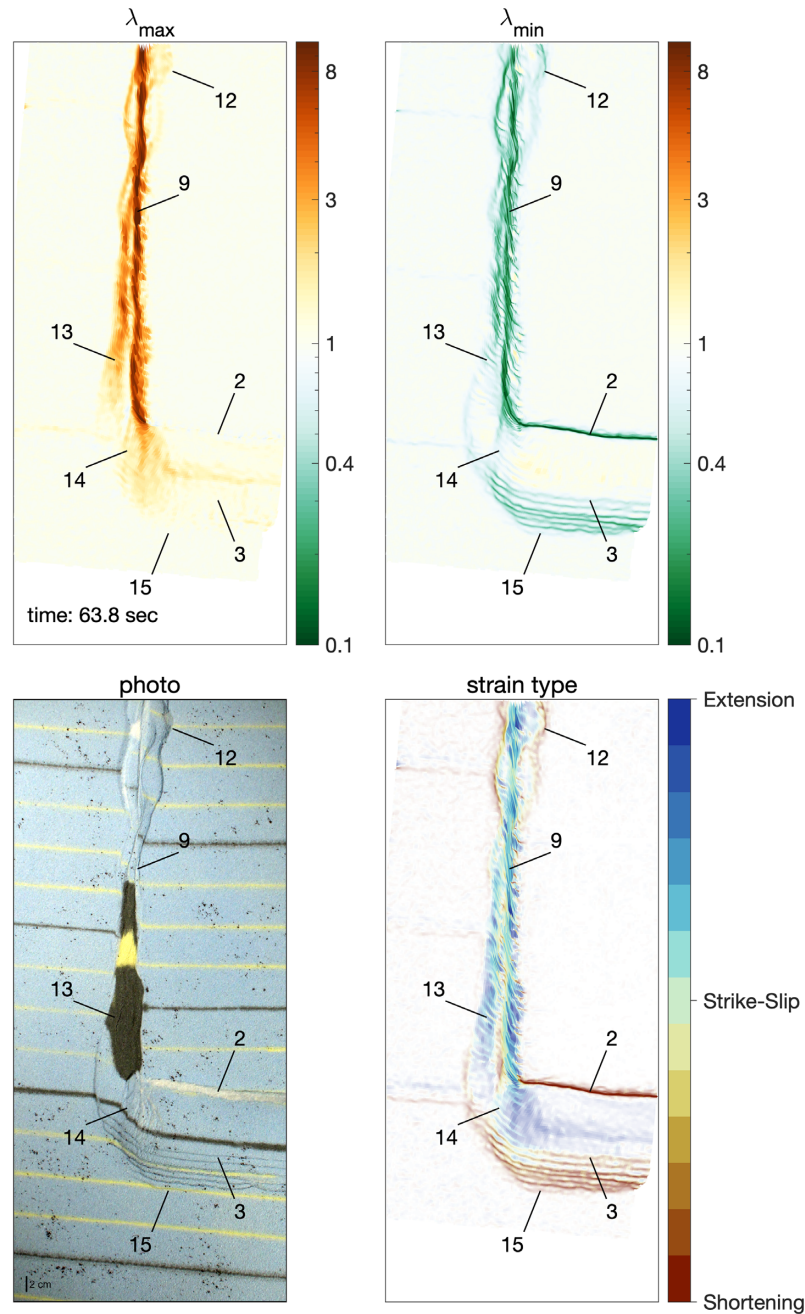
Figure 15. Principal stretches λ_{max}, λ_{min} ($\lambda = 1$ represents no length change) and strain type Φ at the end of the model evolution (63.8 min): shortening (red), strike-slip (green) and extension (blue), with intermediate, oblique deformation at intermediate colours. Numbers indicate: (2) basal thrust; (3) and (15) first and most recent backthrust; (9) main strike-slip fault; (12) transpressional wedge; (13) transtensional basin and (14) normal faulting.

rotation pole, a transtensional basin opens (13) in response to the rotation. There, main dextral-normal faults control the subsidence of the basin, while more distributed oblique-normal slip structures form within the basin (Fig. 16).

At the SW corner of the stable region, approximately N–S oriented normal faults (14) with a dextral slip component, accommodate the transition from the highly elevated thrust wedge in the south and the low topography strike-slip zone along the western margin of the stable region. All of these normal faults are connected with the main N–S oriented strike-slip/transtensional fault. At the end of the experiment, the contractional wedge in the south is composed of the basal thrust (2) that accommodates most of the deformation, and numerous faults in the back thrust system (3). The episodic transfer of shortening towards a newly formed backthrust (15), south of its successor, is visible in video S2 that shows incremental infinitesimal strain and video S4 with strain type. At the same time, distributed extension occurs at the slopes of the wedge (8), see also the visual interpretation from Fig. 16, cross-section c–c'. We also note three straight and alternating E–W striking features west of the deforming area. These features are not due to real deformation, but rather seem to be a PIV-artefact, caused by interference of the contrasting dark marker lines.
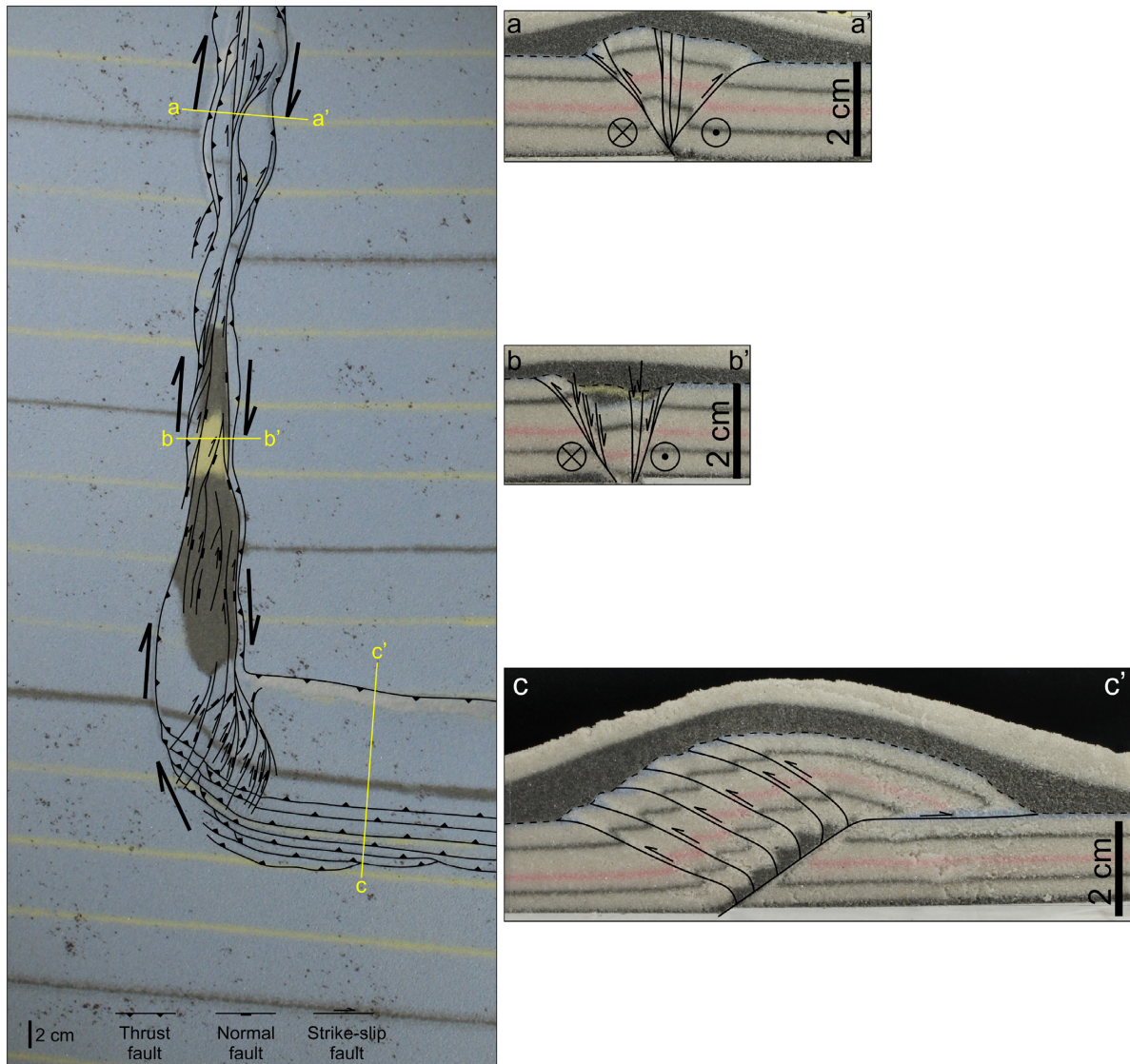
Figure 16. Interpretation of the model in the final state. Left-hand panel: top view with inferred fault structures. The area with dark and yellow sand outlines the basin where we applied sedimentation. Marker lines made with dark or yellow sand visually illustrate the translation of the moving part of the model. Yellow lines overlaying the image show the locations of cross-sections. Right-hand panels: cross-sections at three different locations. The top two sand layers have been added after finalizing the model to stabilize the model topography; the black dashed line indicates the original model topography. Cross-section a–a' (top right) shows the main N-S dextral strike-slip zone, with superimposed thrust faults bounding the strike-slip zone and that formed during the later stage of the model due to rotation. Cross-section b–b' intersects the main N–S dextral strike-slip zone at the location of the opened basin, which is bounded by normal faults. Cross-section c–c' intersects the elevated thrusting wedge, showing six backthrusts, at this location, and the basal thrust that accommodates the largest part of the convergence between the moving domain and the stable region.

5.4 Comparison with visual fault interpretation

To validate that our analysis of the cumulative deformation properly describes the incremental deformation, Fig. 17 (left-hand panel) overlies the final strain type with the faults inferred from the visual inspection of the model surface and the cross-sections. The location of the backthrusts and basal thrust at both sides of the frontal wedge coincides, as does the the gradual transition from the backthrusts towards the N–S strike-slip zone. The inferred strike-slip and strike-slip faults correlate well, and the type of obliquity agrees for transpressional and transtensional regions in the N–S shear zone. We also observe distributed extensional deformation on top of the wedge and NW of the corner—with relatively small magnitudes, see the principal stretches in Fig. 15—where this is not visible in the images due to absence of localized structures.

As an alternative validation of the strain type, we consider the dilatation field, which in 2-D conforms to area change and that provides an additional view on extensional and shortening deformation (whereas it is insensitive to strike-slip). The right-hand panel of Fig. 17 shows that areas of dilatation >1 correspond to areas with extensional strain types (or transtensional) and areas with a dilatation <1 correspond to areas with shortening (or transpressional) strain types.
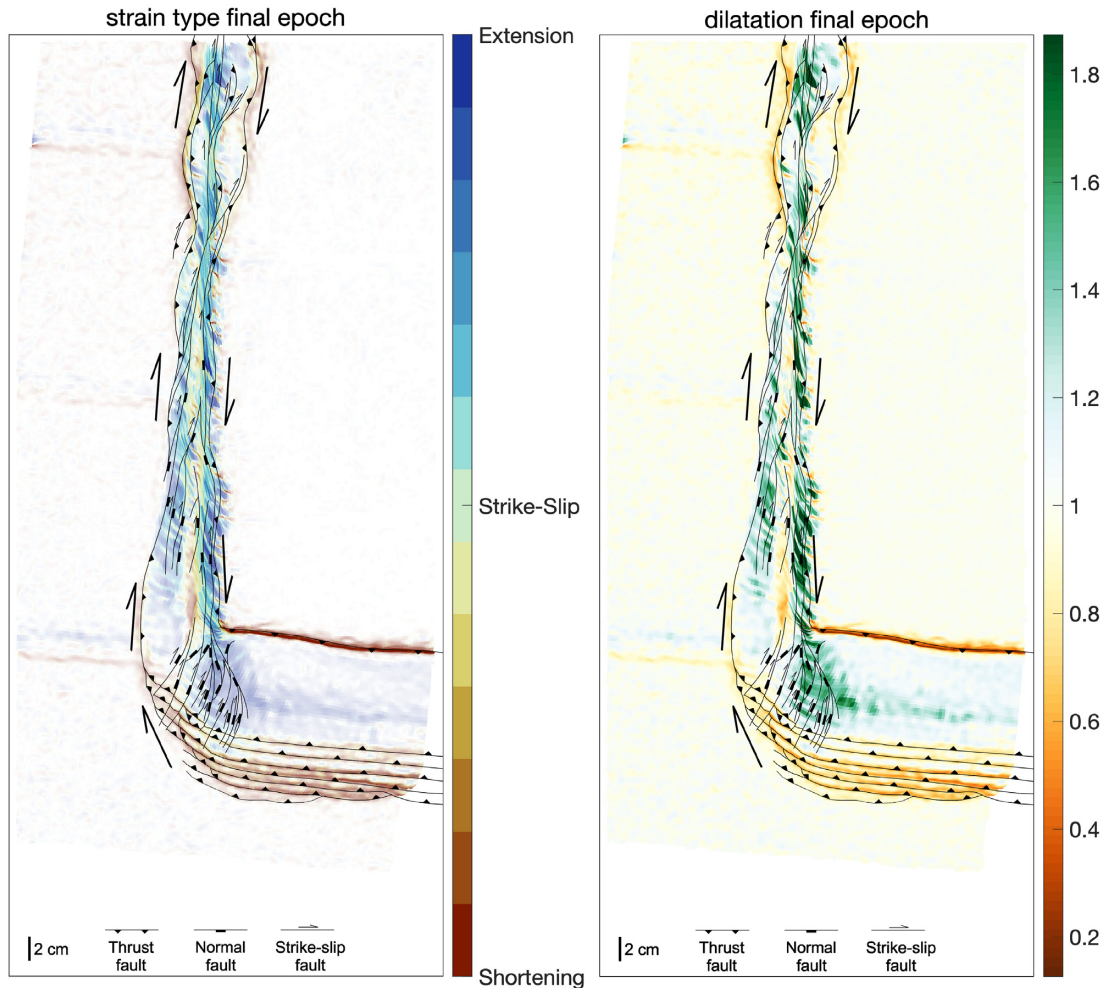
Figure 17. Final deformation, overlain by faults from visual analysis of fault structures, at the end of the model (64 min). Left-hand panel: strain type. Right-hand panel: dilation (relative area change). A dilatation >1 indicates an area increase (extension/transtension) and a dilatation <1 indicates an area decrease (shortening/transpression), it is insensitive to pure strike-slip.

5.5 Time evolution of deformation

We can also analyse the strain type in specific locations as a function of time. This provides a view on when a certain type of deformation was active in a confined material region. Furthermore, it allows to investigate how the strain type evolves when different phases of deformation, with possibly different strain types, affect the cumulative strain type. For this purpose the temporal evolution of cumulative strain type and incremental strain type (based on the incremental strain tensor) can be compared. Figs 18 and 19 show the temporal evolution of the principal stretches, dilatation and the strain types for a selection of points in the model.

The basal thrust

Point *a* (Fig. 18) is positioned in front of the basal thrust (the actual fault is located where multiple W–E material lines have converged), and the evolution of the logarithm of the principal stretches λ (Hencky strains) shows how after 20 min in model time this part of the model is increasingly shortened, $\ln(\lambda_{max})$ stays at a small value (i.e. $\lambda_{max} \approx 1$), while $\ln(\lambda_{min})$ becomes increasingly negative throughout the rest of the model evolution. From the moment of accumulation of significant strain, the strain type refers to continuous shortening. While the incremental strain type is more noisy, from the moment deformation increases, it indicates shortening in a single direction. The cumulative and incremental strain types are thus in agreement for this location. The dilatation (being <1) is consistent with shortening as well, as the surface area decreases gradually at this point.

Back thrusts

We focus on two back thrusts, point *b* focuses on the first back thrust that emerges, point *c* is located on a later fault. We can discern relatively localized deforming regions, even though our method cannot detect discrete faults. The Hencky strains $ln\lambda$ show a single direction
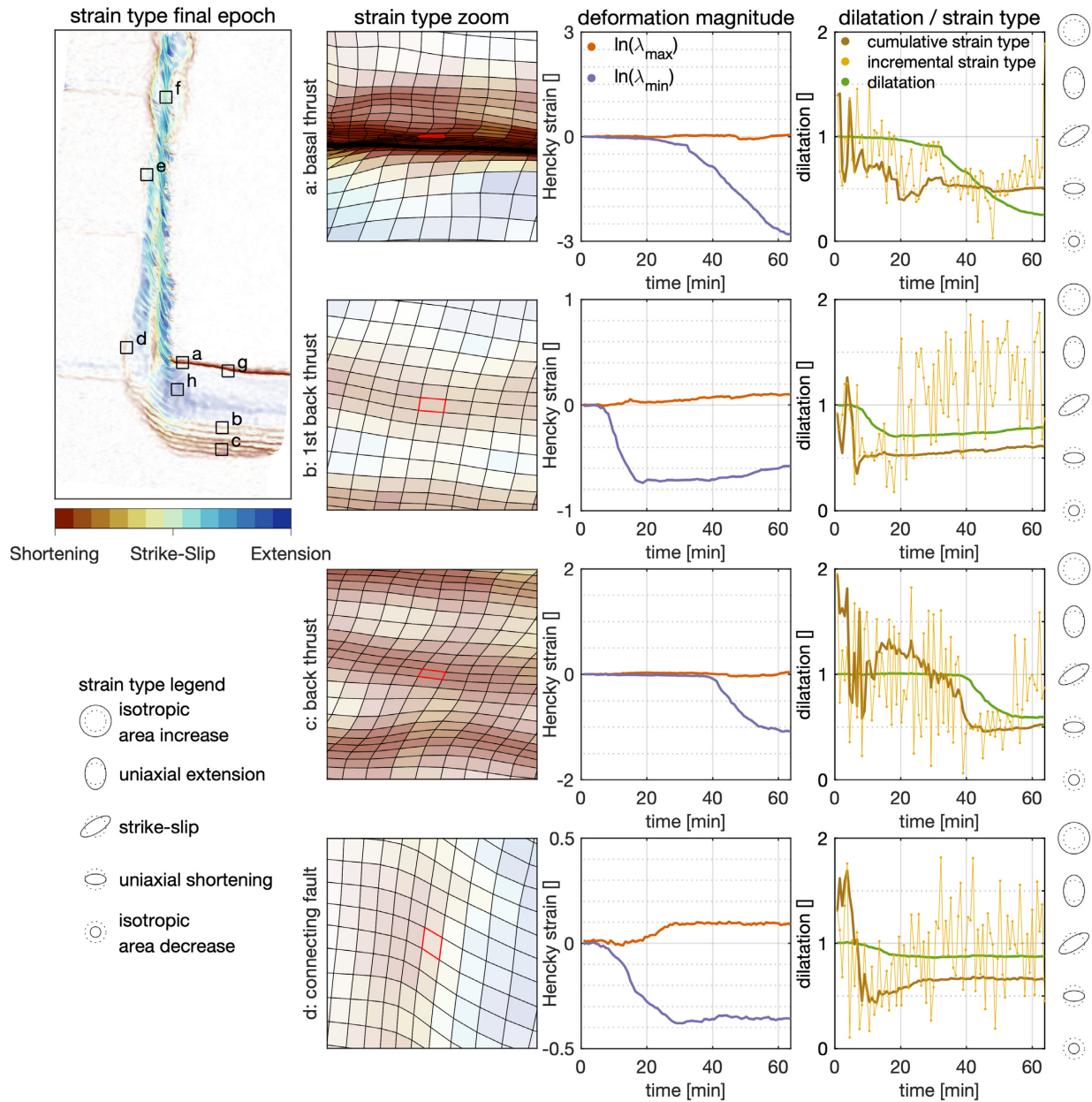
Figure 18. Temporal evolution of principal stretches and strain type as well as dilatation of a few selected points: (a) along the basal thrust; (b) in the first back thrust; (c) in a later back thrust; (d), along the fault that connects the basal thrusts to the strike-slip shear zone. Upper left-hand panel: strain type (final) and overview of the selected areas. Left row: zoom on the strain type and the selected grid cell (which is outlined in red, neighbouring cells outlined in black). Middle row: logarithm of the two principal stretches (Hencky strain) in time. Right row: dilatation (left axis) and strain type (cumulative) and incremental strain type (based on the incremental Lagrange–Green strain, eq. 23) (right axis).

of shortening, with a clear time delay between the start of the model and the start of shortening. During a later phase (after 20 min), the incremental strain type in point *b* hints at transtensional deformation, as the incremental strain type is generally in between strike-slip and extension (right-hand panel). The dominant strain type in both *b* and *c* at the end of the experiment is however shortening, in agreement with the observed thrust faults.

Connection between back thrust and strike-slip zone

From the southernmost back thrust, a thrust fault with oblique slip kinematics (Fig. 16) connects to the strike-slip zone, and we select here point *d*. This point is subject to shortening from 10 min onward until 20 min. From the incremental strain type plot we can see that the deformation becomes more oblique after 20 minutes and gradually becomes strike-slip, which renders the cumulative strain type to oblique shortening (i.e. transpression).
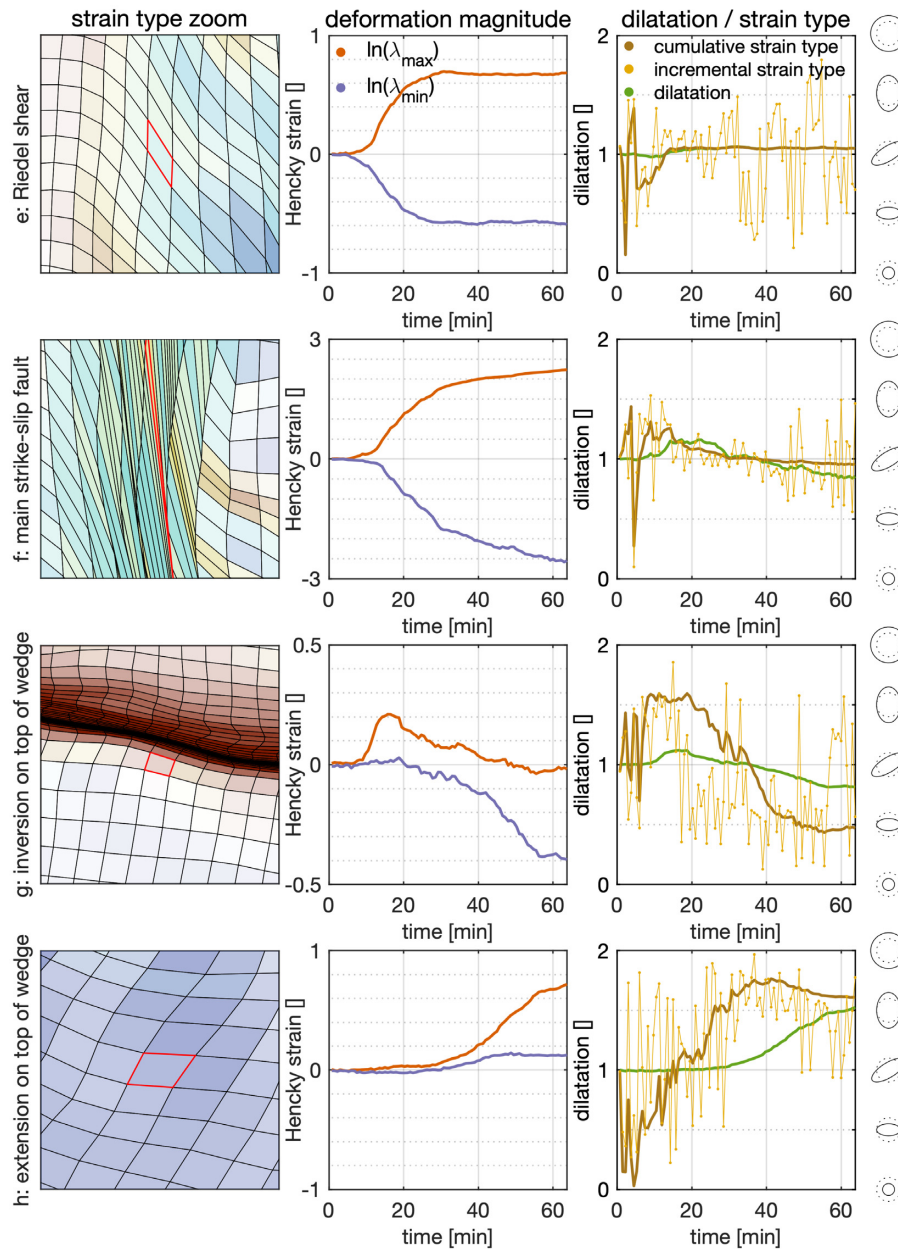
Figure 19. continued. Temporal evolution of principal stretches and strain type as well as dilatation of a few selected points: *e*, in one of the initial Riedel R-shears; *f*, along the main strike-slip fault; *g*, on the wedge close to the basal thrust, where the deformation inverts from extension to shortening (along more or less the same principal direction); *h*, in the extensional area at the western side of wedge. Left row: zoom on the strain type and the selected grid cell. Middle row: logarithm of the principal stretches (Hencky strain) in time. Right row: dilatation (left axis) and strain type (cumulative) and incremental strain type (based on the incremental Lagrange–Green strain, eq. 23) (right axis).

Strike-slip zone

An R-shear, sampled at point *e* (Fig. 19), shows strike-slip activity up to 30 min, after which the principal stretches stay more or less constant. This specific point shows some signs of transtension, while neighbouring points to the west tend to more transpressional deformation. This gradual change in obliquity is well visible in the other direction: points to the east contain a larger fraction of extensional deformation. The strike-slip motion migrates further east after the R-shears connect (see the differences between Figs 13 and 14). Point *f* lies within the main strike-slip fault, and shows most of the time purely strike-slip motion, exemplified by the equal magnitude of the two Hencky strains $ln\lambda$. Only at the end the dilatation diverges slightly from 1.

Extension on the thrust wedge

At the edges of the thrust wedge, we find distributed and localized extension. Distributed extension at the northern side of the wedge, where point *g* initially shows extension as the largest Hencky strain is positive. After 20 min the influence of the basal thrust becomes noticeable, and the negative Hencky strain becomes the largest in magnitude. Both dilatation and strain type show this reversal. The incremental strain type, even though it is more noisy, shows this reversal, approximately 10 min before the extensional deformation is balanced by shortening deformation in the cumulative strain (right-hand panel). At the transitional region between the high topography wedge and low topography strike-slip region, we find point *h*, in a region with abundant normal faulting (Fig. 17). As both Hencky strains are positive, this point is subject to bi-axial extension. The varying orientation of the normal faults in this area, Fig. 17, also hint at extension in more than one direction.

6 DISCUSSION

6.1 Following material during translation, rotations and shape changes

The method that we apply to follow the displacement of material through time (e.g. Senatore *et al.* 2013; Stanier *et al.* 2016; Boutelier *et al.* 2019; Krÿza *et al.* 2019), building on spatial velocity fields derived from imagery (PIV), makes it possible to study deformation of a small piece of material in an environment that is subject to large translations, rotations or shape changes. Compared to the method of Boutelier *et al.* (2019) we improve the determination of the displacement gradient by using a bilinear interpolation through shape functions (appendix A), which takes into account the gradual geometry change of the grid, similar as Senatore *et al.* (2013). By tracing material points in time we can also determine the cumulative deformation, thereby increasing the signal-to-noise ratio significantly with respect to the incremental strain. This is shown by our application to PIV-derived velocities of the analogue model of tectonic deformation. The time evolution of the stretch tensor $\mathbf{V}$ and the rotation angle θ in Video S3 contains much less noise compared to the incremental strain tensor ϵ and the accompanying rotation ω in Video S2.

We observe that the displacement in an area that does neither translate nor deform (the indenter) is almost normally distributed and unbiased, having a near zero mean. Such random PIV displacement errors lead to random walk noise in integrated Lagrangian displacements (Stanier *et al.* 2016). The standard deviation of the integrated displacement error grows by $\sigma_u = \sqrt{n}\sigma_{u_i}$, with n the number of epochs and σ_{u_i} the standard deviation of the incremental displacement error. PIV displacement errors are larger for moving areas compared to stagnant areas (Thielicke 2014); non-deforming but translating regions may therefore be more indicative for uncertainties of strain derived from displacements. We observe that in solely translating areas (southwest corner of the model) the strain is nearly normally distributed, and centered around zero. Similarly, the finite stretch is again semi-normally distributed, where its standard deviation increases in time by approximately $\sqrt{n}$. In this region we find that the incremental strain has $\sigma_{\epsilon_i} \approx 6 \times 10^{-3}$, the standard deviation of the finite stretch error increases to $\sigma_V \approx 5 \times 10^{-2}$ at the end of the model run. The $\sqrt{n}$ factor implies that the signal-to-noise ratio improves for continuously deforming regions, whereas it gradually deteriorates for regions with discontinued deformation. Furthermore, strain in shear zones may be underestimated for narrow zones, as PIV tends to distribute displacement over larger areas when the interrogation window is comparable in width or wider than the shear zone (Boutelier *et al.* 2019). Next, PIV displacement errors are larger in shearing areas (Thielicke 2014; Stanier *et al.* 2016), which makes it difficult to extrapolate strain errors from non-deforming areas to areas undergoing large deformation. Still, integration of random errors in the cumulative stretch reduces the errors from incremental displacements, exemplified by the much sharper and clearer patterns of finite deformation compared to those from the incremental deformation.

Creating Lagrangian displacements requires continuity of the tracked particle path, which means that for areas missing Eulerian displacements the construction of Lagrangian displacements is discontinued (PIVlab applies interpolation for areas with outliers (Thielicke 2014), which is an acceptable solution when regions with outliers are small). Stanier *et al.* (2016) provide a solution for temporary data gaps, by integrating PIV and the estimation of Lagrangian displacements, while applying PIV not strictly sequential. In this PIV approach, the reference image is not updated every time step, but only when the loss cross-correlation, due to cumulative deformation, is becoming too large. Such an approach would also allow for mitigating displacement data gaps.

6.2 Correct strain tensors for large deformation

We base our deformation analysis on the left-stretch tensor $\mathbf{V}$ that gives an exact description of the shape change that is described by the displacement gradient (Section 2.5.3). Importantly, $\mathbf{V}$ is insensitive to rigid body rotations. The principal values from $\mathbf{V}$ (or from right-stretch tensor $\mathbf{U}$) describe the true length changes along the principal axes. Recently, Boutelier *et al.* (2019)) described PIV-derived finite deformation by $\mathbf{U}$. Contrastingly, the infinitesimal strain tensor ϵ (eq. 15) that has often been used to describe relatively large deformations (e.g. Hoth *et al.* 2007; Adam *et al.* 2013; Sun *et al.* 2018; Poppe *et al.* 2019; Schellart *et al.* 2019), describes shape changes properly only for small shears and small rotations. Especially, quantities such as principal strains, area change and rotation from the infinitesimal strain tensor no longer hold for large shear (Section 2.5.4). For example, the rotation ω (eq. 17) applied to large deformations may lead to values that indicate $>2\pi$ rotations (Fig. 5), which is not possible with stationary strike-slip faults. In the absence of additional rigid body rotations, while the rotation value itself implies an incorrect rotation beyond values $>\pi/2$, its value can still be proportional to a shear γ (as long as there are no additional rotations, such as in Adam *et al.* (2013)). The degree to which infinitesimal strains lead to qualitatively wrong inferences, will thus

depend on the setting. Similarly, the use divergence ($\epsilon_{xx} + \epsilon_{yy}$) (Schellart *et al.* 2019) or dilatation using ϵ, to discriminate between areas of area increase or decrease, may lead to misinterpretations for large shear strains (Fig. 5).

6.3 Strain classification

For small strains, the type of strain (e.g. extension, shortening or strike-slip) can be determined from principal strains in a straightforward way (Kreemer *et al.* 2014). However, for large strains this distinction between different types of strain can no longer be made based on comparison of principal strains in a similar manner. We introduce the use of Hencky strains (logarithm of finite principal stretch, Section 2.7) to characterize strain type. Doing so, we avoid the problem of changing ratios of principal stretches in finite shear deformation (i.e. strike-slip in the horizontal plane), that occurs even for deformation that is constant in time (Fig. 7). Hencky strains provide a constant ratio for the two principal strains for extension, strike-slip (simple or pure shear) and shortening, irrespective of the amount of deformation (Fig. 7). For oblique deformation this ratio only slightly changes with increasing deformation, but for our qualitative measure of strain type we argue this is only a minor issue. Our definition of strain type provides the same qualitative characterization of deformation, as the deformation classification based on visual inspection of fault patterns (Fig. 17). More so, it provides a fully automated, temporal evolution of deformation magnitude and strain type, and it is able to detect distributed deformation that does not lead to recognizable structures.

Scale dependence of pure shear

Our strain type provides the same interpretation for pure shear as well as simple shear in the horizontal plane (or combinations thereof as sub-simple shear), as the relative magnitudes of the two Hencky strains will be the same for all types of isochoric shear: $\ln \lambda_{\max} = -\ln \lambda_{\min}$. While the mean rotation in pure shear is zero, and in simple shear all material lines rotate except for the lines parallel with the direction of shear, this has no effect on the strain type measure. Namely, our strain type measure only considers principal strain magnitudes, and does not take into account principal direction changes. Even though pure shear in the horizontal plane may describe the style of deformation at large scale, at smaller scales the presence of pure shear depends on whether this deformation localizes on faults or that deformation is distributed. For example, the collision of India into Asia leads to both shortening in the convergence direction, as well as an orthogonal extension, leading to extrusion of the indented Asia (Tapponnier *et al.* 1982). Such a deformation has at the large scale a strong pure shear component in the horizontal plane (Fossen 2016), while at smaller scales the roughly E–W extrusion is accommodated by strike-slip faults and normal faults, even though there is long-standing debate on what structures accommodate the extension (Searle *et al.* 2011; Wallis & Searle 2019). A similar process of extrusion involving pure shear, where the escape of material occurs along (conjugate) strike-slip faults is found for the Eastern Alps (Ratschbacher *et al.* 1991; van Gelder *et al.* 2017).

For crustal tectonics pure shear has thus a large scale dependence, where the necessity to discriminate between simple shear and pure shear reduces when shear due to individual faults can be observed. When deformation is partitioned on individual faults, which accommodate deformation by (oblique) strike-slip or normal or reverse faulting, our strain type will have no difficulty in describing those deformations (as long as the spatial resolution is sufficient to discriminate individual structures). Only an area undergoing pure shear in a continuous sense (without faults), for example in a ductile manner, or as elastic deformation (at small strains), is interpreted in our strain measure equally as simple shear.

Strain type for subsequent phases of deformation

When asking the question whether cumulative deformation gives a good sense of episodical deformation related to slip on faults, we see in our analogue experiments that the final strain type agrees with almost all inferred types of faults. Our strain measure based on logarithmic stretch provides a way of assessing the type of deformation, either distributed, or localized (i.e. faulting), provided that no inversion of deformation takes place. The finite stretch contains no information on the deformation path, so if for example left-lateral strike-slip faulting is followed by right-lateral strike-slip on the same structure, or extension is succeeded by shortening (see point *g* in Fig. 19), the cumulative strain type will not be representative for the deformation as occurred during the full observation period. Also, episodical deformation such as the Riedel shears in the analogue model can be suppressed in the total deformation. In a similar way, shortening followed by a phase with strike-slip (see point *d* in Fig. 18) is in the finite deformation indistinguishable from concurrent strike-slip and shortening (transpression). In these instances, it would be preferred to divide the observation period into separate phases (each with its own deformation gradient **F**) to account for opposite styles of deformation, while still making advantage of the integration of deformation that reduces the noise that may be dominant in incremental deformation.

Previous approaches to interpret strain

The interpretation of a strain tensor is non-trivial, as tensor components strongly depend on the orientation of the reference frame (Section 2.5.3). Diagonal components and off-diagonal components of the strain tensor are communicative, and vary according to the reference orientation. Often in analogue modeling studies, strain is interpreted by inspecting individual strain tensor components, to derive extensional

or shear components (e.g. Adam *et al.* 2005; Fischer & Keating 2005; Hoth *et al.* 2007; Boutelier & Oncken, 2011; Chen *et al.* 2015; Le Corvec *et al.* 2014; Galland *et al.* 2016; Barcos *et al.* 2016). This approach is valid only when all deformation zones align with the Cartesian reference frame, which limits the use to relatively simple models with straight and perpendicular deformation structures. Contrastingly, principal stretches or strains are unique for a given deformation and have been used to analyse deformation in analogue models by Haq & Davis (2009). Still, principal strains or stretches are inconclusive on shear contributions (in the horizontal plane: strike-slip). Likewise, dilatation can be used as a measure for shortening or extensional deformation (Kettermann *et al.* 2016), but it is insensitive to shear. In the absence of rigid body rotation, infinitesimal rotation ω (eq. 17) can be used to map small simple shears along strike-slip faults (Le Corvec & Walter 2009; Hatem *et al.* 2017). However, for large deformations, ω is no longer proportional to the mean rotation of material (Fig. 5). Even though maximum shear strain γ_{max} will highlight shear zones (e.g. Cruz *et al.* (2008)), it is just as well sensitive to shortening or extensional deformation. Different from the aforementioned approaches, our method can be applied to any deformation zone orientation, and is independent from the chosen reference frame.

6.4 Decomposition of strain

In this study, we have developed a qualitative classification of strain, but we do not quantitatively decompose deformation into contributions of shearing and extensional deformation. In recent literature there are multiple efforts to decompose deformation into contributions of shear, extension and rotation. Wang *et al.* (2019) aim to separate rotations induced by shearing motions and rigid body rotations, based on analysis of the minimum angular velocity in all directions in a small volume, called the Liutex method. Holmedal (2020) applies this model to deformation of solids. The Liutex method however relies on the implicit assumption that shear rotations and rigid body rotations act in the same direction (i.e. the induced vorticity or spin has the same sign). One could imagine a combination of a right-lateral strike-slip fault, inducing a clockwise rotation within the shear zone, combined with a counter-clockwise rigid body motion. Such combination of opposing rotations can be found in the Dinarides, where right-lateral strike-slip (van Unen *et al.* 2019) occurred simultaneously with counter-clockwise rotations of Adria (Marton *et al.* 2003). Furthermore, as the Liutex model does not consider extensional motions, even though extensional motions induce internal angular velocities as well (Allmendinger *et al.* 2011), it is of limited use for decomposing the deformation of solid materials.

Other studies derived decompositions of a 3-D deformation gradient into a succession of a single, volume preserving extension, a simple shear, a rotation and a dilatation (Wang 1996), or alternatively, a dilation, a rotation and two simple shears (Zheng *et al.* 2000). As a description of tectonic deformation in the horizontal (2-D) plane requires the inclusion of two orthogonal extensions, we cannot use these decompositions to describe tectonic deformation in a physically meaningful way.

A recent, promising decomposition of deformation is the QR decomposition of **F** that allows for a separation of deformation into simple shear, extension and rotation contributions (Srinivasa 2012; Freed *et al.* 2019, see eqs 11 and 12). For 2 dimensions, the extension contribution includes two orthogonal components and a single simple shear contribution, together named the Laplace stretch. In Section 2.4, we apply this scheme to describe a general deformation in the direction of the chosen reference Cartesian axes. In two dimensions, this implies that the decomposed simple shear is always parallel to the *x*-axis. To describe shear in the horizontal plane on strike-slip faults, we would thus first have to locally align the *x*-axis of our reference frame with each fault to obtain a meaningful decomposition of deformation. Namely, the QR decomposition is possible in any chosen reference axis orientation (Freed & Srinivasa 2015). This implies the development of a spatially and temporally varying definition of the reference axes, and we do not pursue that in this work as it would require the automatic detection of fault structures. The Laplace stretch bears many similarities to the deformation tensor **D** used in structural geology (e.g. Fossen 2016), which can be constructed when the orientation of a shear zone is known. Similarly, deriving slip orientations on faults (e.g. Leever *et al.* 2011) from displacement fields requires a prior definition of fault orientations. As such this method works only when the spatial derivative of the displacement field is determined perpendicular to a fault.

Hence, due to current unavailability of methods that allow a unique decomposition of deformation into a shear and two orthogonal extension deformations (as in Fig. 3), our strain type measure provides an alternative in the form of a qualitative descriptor of the relative amounts of shear and extensional (or shortening) deformation. For describing the magnitude of strain, we can still resort to the established principal stretches λ (eq. 31) based on the left-stretch tensor **V** that can easily be related to principal strains, even though the principal stretches are inconclusive to the type of strain.

6.5 Outlook

In this study, we have made use of an initial grid that is homogeneous throughout the full area of interest. During the subsequent time steps the grid gradually deforms, which leads in general to an inhomogeneous spatial resolution of the derived deformation fields, as extensional or shortening stretches have opposite effects on the grid side lengths. To prevent overly loss of spatial resolution in extensional areas (including shear zones) we have implemented an homogeneous grid refinement with respect to the resolution of the displacement fields as provided by the image correlation techniques. An efficient method to cope with the spatial resolution gradually becoming more inhomogeneous in deforming areas is to use unstructured meshes that are initially inhomogeneous, with increased resolution in deforming regions. This suggests the use of triangular meshes, for which the shape functions can be easily adapted.

While we apply our strain measure in a context of analogue models of crustal tectonics, we think it has a potential to describe large strains in high resolution displacement inversions of geodetic data of coseismic displacements (Lauer *et al.* 2020), geodetically observed strain rates of glaciers (Lhermitte *et al.* 2020) or interpretation of 2-D deformation in numerical geodynamic models.

7 CONCLUSIONS

We have applied methods to update Lagrangian material displacements using incremental, space-based (Eulerian) displacements from image correlation techniques. We show that the resulting displacement fields can be used to map high resolution strain fields involving large and complex deformations.

In a similar way as for small strains, it is possible to use principal stretches to classify the type of strain that has led to finite deformation. For this purpose, we introduce a novel use of logarithmic principal stretches, also known as Hencky strains, to qualitatively describe 2-D plane deformation. Hencky strains have the desired property that the relative lengths between the two principal strains do not change during constant incremental deformation.

Tectonic deformation, that is shortening, strike-slip or extension and their transpressional and transtensional transitions, can be adequately described using our developed qualitative strain type measure. Due to the temporal and spatial continuous description, this measure can be used to inspect the temporal evolution of strain, even in the absence of discrete structures.

AVAILABILITY OF DATA

The data underlying this article (top-view and side-view images) are available in the Yoda data repository of the Utrecht University (Broerse *et al.* 2021). The software to process displacement fields to obtain strain fields can be obtained at https://doi.org/10.5281/zenodo.4529475.

CReDiT
Author contributions following the CReDiT taxonomy:
Conceptualization: T.B.
Formal analysis: N.K. (PIV)
Investigation: T.B.
Methodology: T.B. C.K.
Resources : N.K., E.W. (analogue model)
Software: T.B.
Validation: T.B., C.K., N.K.
Supervision: T.B.
Visualization: T.B., N.K.
Writing - original draft: T.B., N.K.
Writing - review & editing T.B., N.K., C.K., E.W.

REFERENCES

Adam, J., Klinkmüller, M., Schreurs, G. & Wieneke, B., 2013. Quantitative 3D strain analysis in analogue experiments simulating tectonic deformation: Integration of X-ray computed tomography and digital volume correlation techniques, *J. Struct. Geol.,* **55,** 127–149.

Adam, J. *et al.*, 2005. Shear localisation and strain distribution during tectonic faulting—new insights from granular-flow experiments and high-resolution optical image correlation techniques, *J. Struct. Geol.,* **27**(2), 283–301.

Allmendinger, R.W., Cardozo, N. & Fisher, D.M., 2011. *Structural Geology Algorithms: Vectors and Tensors,* Cambridge Univ. Press.

Barcos, L., Díaz-Azpiroz, M., Balanyá, J., Expósito, I., Jiménez-Bonilla, A. & Faccenna, C., 2016. Analogue modelling of inclined, brittle–ductile transpression: testing analytical models through natural shear zones (external Betics), *Tectonophysics,* **682,** 169–185.

Boutelier, D. & Oncken, O., 2011. 3-D thermo-mechanical laboratory modeling of plate-tectonics: modeling scheme, technique and first experiments, *Solid Earth,* **2**(1), 35.

Boutelier, D., Schrank, C. & Regenauer-Lieb, K., 2019. 2-D finite displacements and strain from particle imaging velocimetry (PIV) analysis of tectonic analogue models with TecPIV, *Solid Earth,* **10**(4), 1123–1139.

Broerse , T., Krstekanić , N. & Willingshofer , E., 2021. Data supplement to: Mapping and classifying large deformation from digital imagery: application to analogue models of lithosphere deformation, *Data publication platform of Utrecht University,* https://doi.org/10.24416/UU01-LN58S4.

Brun, J.-P., 2002. Deformation of the continental lithosphere: insights from brittle-ductile models, *Geol. Soc., Lond., Spec. Publ.,* **200**(1), 355–370.

Cardozo, N. & Allmendinger, R.W., 2009. SSPX: a program to compute strain from displacement/velocity data, *Comp. Geosci.,* **35**(6), 1343–1357.

Charalampidou, E.-M., Hall, S.A., Stanchits, S., Lewis, H. & Viggiani, G., 2011. Characterization of shear and compaction bands in a porous sandstone deformed under triaxial compression, *Tectonophysics,* **503**(1–2), 8–17.

Chen, Z., Schellart, W.P. & Duarte, J.C., 2015. Quantifying the energy dissipation of overriding plate deformation in three-dimensional subduction models, *J. geophys. Res.,* **120**(1), 519–536.

Crameri, F., 2018. Scientific colour-maps. Zenodo, doi:10.5281/zenodo.1243862.

Cruz, L., Teyssier, C., Perg, L., Take, A. & Fayon, A., 2008. Deformation, exhumation, and topography of experimental doubly-vergent orogenic wedges subjected to asymmetric erosion, *J. Struct. Geol.,* **30**(1), 98–115.

Duarte, J.C., Schellart, W.P. & Cruden, A.R., 2013. Three-dimensional dynamic laboratory models of subduction with an overriding plate and variable interplate rheology, *Geophys. J. Int.,* **195**(1), 47–66.

Fischer, M.P. & Keating, D.P., 2005. Photogrammetric techniques for analyzing displacement, strain, and structural geometry in physical models: application to the growth of monoclinal basement uplifts, *GSA Bulletin,* **117**(3–4), 369–382.

Fossen, H., 2016. *Structural Geology,* Cambridge Univ. Press.

Fossen, H., Tikoff, B. & Teyssier, C., 1994. Strain modeling of transpressional and transtensional deformation, *Norsk geologisk tidsskrift,* **74**(3), 134–145.

Freed, A. & Srinivasa, A., 2015. Logarithmic strain and its material derivative for a QR decomposition of the deformation gradient, *Acta Mech.,* **226**(8), 2645–2670.

Freed, A.D., le Graverend, J.-B. & Rajagopal, K., 2019. A decomposition of Laplace stretch with applications in inelasticity, *Acta Mech.,* **230**(9), 3423–3429.

Funiciello, F., Moroni, M., Piromallo, C., Faccenna, C., Cenedese, A. & Bui, H.A., 2006. Mapping mantle flow during retreating subduction: laboratory models analyzed by feature tracking, *J. geophys. Res.,* **111**(B3), doi:10.1029/2005JB003792.

Galland, O., Bertelsen, H.S., Guldstrand, F., Girod, L., Johannessen, R.F., Bjugger, F., Burchardt, S. & Mair, K., 2016. Application of open-source photogrammetric software MicMac for monitoring surface deformation in laboratory models, *J. geophys. Res.,* **121**(4), 2852–2872.

Gomes, A., Rosas, F., Duarte, J., Schellart, W., Almeida, J., Tomás, R. & Strak, V., 2019. Analogue modelling of brittle shear zone propagation across upper crustal morpho-rheological heterogeneities, *J. Struct. Geol.,* **126**, 175–197.

Guillaume, B., Husson, L., Funiciello, F. & Faccenna, C., 2013. The dynamics of laterally variable subductions: laboratory models applied to the Hellenides, *Solid Earth,* **4**(2), 179–200.

Hall, S.A., Wood, D.M., Ibraim, E. & Viggiani, G., 2010. Localised deformation patterning in 2D granular materials revealed by digital image correlation, *Granular Matter,* **12**(1), 1–14.

Hampel, A., Adam, J. & Kukowski, N., 2004. Response of the tectonically erosive south Peruvian forearc to subduction of the Nazca Ridge: analysis of three-dimensional analogue experiments, *Tectonics,* **23**(5), doi:10.1029/2003TC001585.

Haq, S.S. & Davis, D.M., 2009. Interpreting finite strain: analysis of deformation in analog models, *J. Struct. Geol.,* **31**(7), 654–661.

Hatem, A.E., Cooke, M.L. & Toeneboehn, K., 2017. Strain localization and evolving kinematic efficiency of initiating strike-slip faults within wet kaolin experiments, *J. Struct. Geol.,* **101**, 96–108.

Hoger, A. & Carlson, D.E., 1984. Determination of the stretch and rotation in the polar decomposition of the deformation gradient, *Quater. Appl. Math.,* **42**(1), 113–117.

Holmedal, B., 2020. Spin and vorticity with vanishing rigid-body rotation during shear in continuum mechanics, *J. Mech. Phys. Solids,* **137**, 103835, doi:10.1016/j.jmps.2019.103835.

Hoth, S., Hoffmann-Rothe, A. & Kukowski, N., 2007. Frontal accretion: an internal clock for bivergent wedge deformation and surface uplift, *J. geophys. Res.,* **112**(B6), doi:10.1029/2006JB004357.

Hubert-Ferrari, A., King, G., Manighetti, I., Armijo, R., Meyer, B. & Tapponnier, P., 2003. Long-term elasticity in the continental lithosphere; modelling the Aden Ridge propagation and the Anatolian extrusion process, *Geophys. J. Int.,* **153**(1), 111–132.

Hughes, T.J., 2012. *The Finite Element Method: Linear Static and Dynamic Finite Element Analysis,* Courier Corporation.

Kääb, A., Altena, B. & Mascaro, J., 2017. Coseismic displacements of the 14 November 2016 Mw 7.8 Kaikoura, New Zealand, earthquake using the Planet optical cubesat constellation, *Nat. Haz. Earth Syst. Sci.,* **17**, 627–639.

Kettermann, M., von Hagke, C., van Gent, H.W., Grützner, C. & Urai, J.L., 2016. Dilatant normal faulting in jointed cohesive rocks: a physical model study, *Solid Earth,* **7**, 843–856.

Kreemer, C., Blewitt, G. & Klein, E.C., 2014. A geodetic plate motion and global strain rate model, *Geochem., Geophys., Geosyst.,* **15**(10), 3849–3889.

Kryza, O., Závada, P. & Lexa, O., 2019. Advanced strain and mass transfer analysis in crustal-scale oroclinal buckling and detachment folding analogue models, *Tectonophysics,* **764**, 88–109.

Lauer, B., Grandin, R. & Klinger, Y., 2020. Fault geometry and slip distribution of the 2013 Mw 7.7 Balochistan earthquake from inversions of SAR and optical data, *J. geophys. Res.,* **125**(7), doi:10.1029/2019JB018380.

Le Corvec, N. & Walter, T.R., 2009. Volcano spreading and fault interaction influenced by rift zone intrusions: insights from analogue experiments analyzed with digital image correlation technique, *J. Volc. Geotherm. Res.,* **183**(3–4), 170–182.

Le Corvec, N., Walter, T.R., Ruch, J., Bonforte, A. & Puglisi, G., 2014. Experimental study of the interplay between magmatic rift intrusion and flank instability with application to the 2001 Mount Etna eruption, *J. geophys. Res.,* **119**(7), 5356–5368.

Leever, K.A., Gabrielsen, R.H., Sokoutis, D. & Willingshofer, E., 2011. The effect of convergence angle on the kinematic evolution of strain partitioning in transpressional brittle wedges: Insight from analog modeling and high-resolution digital image analysis, *Tectonics,* **30**(2), doi:10.1029/2010TC002823.

Lenoir, N., Bornert, M., Desrues, J., Bésuelle, P. & Viggiani, G., 2007. Volumetric digital image correlation applied to X-ray microtomography images from triaxial compression tests on argillaceous rock, *Strain,* **43**(3), 193–205.

Lhermitte, S., Sun, S., Shuman, C., Wouters, B., Pattyn, F., Wuite, J., Berthier, E. & Nagler, T., 2020. Damage accelerates ice shelf instability and mass loss in Amundsen Sea Embayment, *Proc. Natl. Acad. Sci.,* **117**(40), 24 735–24 741.

Malvern, L.E., 1969. *Introduction to the Mechanics of a Continuous Medium,* Pearson.

Mao, L. & Chiang, F.-P., 2016. 3D strain mapping in rocks using digital volumetric speckle photography technique, *Acta Mech.,* **227**(11), 3069–3085.

Marton, E., Drobne, K., Ćosović, V. & Moro, A., 2003. Palaeomagnetic evidence for Tertiary counterclockwise rotation of Adria, *Tectonophysics,* **377**(1–2), 143–156.

Means, W., 1989. Stretching faults, *Geology,* **17**(10), 893–896.

Morishita, Y., Kobayashi, T., Fujiwara, S. & Yarai, H., 2017. Complex Crustal deformation of the 2016 Kaikoura, New Zealand, earthquake revealed by ALOS-2 complex crustal Deformation of the 2016 Kaikoura, New Zealand, earthquake revealed by ALOS-2, *Bull. seism. Soc. Am.,* **107**(6), 2676–2686.

Nilforoushan, F., Koyi, H.A., Swantesson, J.O. & Talbot, C.J., 2008. Effect of basal friction on surface and volumetric strain in models of convergent settings measured by laser scanner, *J. Struct. Geol.,* **30**(3), 366–379.

Poppe, S. *et al.*, 2019. An inside perspective on magma intrusion: quantifying 3D displacement and strain in laboratory experiments by dynamic X-ray computed tomography, *Front. Earth Sci.,* **7**, 62, doi:10.3389/feart.2019.00062.

Ramberg, H., 1975. Particle paths, displacement and progressive strain applicable to rocks, *Tectonophysics,* **28**(1–2), 1–37.

Ratschbacher, L., Merle, O., Davy, P. & Cobbold, P., 1991. Lateral extrusion in the Eastern Alps, part 1: boundary conditions and experiments scaled for gravity, *Tectonics,* **10**(2), 245–256.

Rutter, E., Faulkner, D. & Burgess, R., 2012. Structure and geological history of the Carboneras Fault Zone, SE Spain: part of a stretching transform fault system, *J. Struct. Geol.,* **45**, 68–86.

Sanderson, D.J. & Marchini, W., 1984. Transpression, *J. Struct. Geol.,* **6**(5), 449–458.

Schellart, W., Chen, Z., Strak, V., Duarte, J. & Rosas, F., 2019. Pacific subduction control on Asian continental deformation including Tibetan extension and eastward extrusion tectonics, *Nat. Commun.,* **10**(1), 1–15.

Schellart, W., Jessell, M. & Lister, G., 2003. Asymmetric deformation in the backarc region of the Kuril arc, northwest Pacific: new insights from analogue modeling, *Tectonics,* **22**(5), doi:10.1029/2002TC001473.

Schellart, W.P. & Strak, V., 2016. A review of analogue modelling of geodynamic processes: approaches, scaling, materials and quantification, with an application to subduction experiments, *J. Geodyn.,* **100,** 7–32.

Searle, M.P., Elliott, J., Phillips, R. & Chung, S.-L., 2011. Crustal–lithospheric structure and continental extrusion of Tibet, *J. Geol. Soc.,* **168**(3), 633–672.

Senatore, C., Wulfmeier, M., Vlahinić, I., rade, J. & Iagnemma, K., 2013. Design and implementation of a particle image velocimetry method for analysis of running gear–soil interaction, *Journal of Terramechanics,* **50**(5–6), 311–326.

Sotiris, V., Athanassios, G., Varvara, T. & Aggeliki, B., 2018. A preliminary report on the M7.5 Palu 2018 earthquake co-seismic ruptures and landslides using image correlation techniques on optical satellite data, Report submitted to EMSC on 19 October 2018 12:00 UTC.

Srinivasa, A., 2012. On the use of the upper triangular (or QR) decomposition for developing constitutive equations for Green-elastic materials, *Int. J. Eng. Sci.,* **60,** 1–12.

Stanier, S.A., Blaber, J., Take, W.A. & White, D., 2016. Improved image-based deformation measurement for geotechnical applications, *Can. Geotech. J.,* **53**(5), 727–739.

Strak, V. & Schellart, W.P., 2014. Evolution of 3-D subduction-induced mantle flow around lateral slab edges in analogue models of free subduction analysed by stereoscopic particle image velocimetry technique, *Earth planet. Sci. Lett.,* **403,** 368–379.

Sun, M., Yin, A., Yan, D., Ren, H., Mu, H., Zhu, L. & Qiu, L., 2018. Role of pre-existing structures in controlling the Cenozoic tectonic evolution of the eastern Tibetan plateau: new insights from analogue experiments, *Earth planet. Sci. Lett.,* **491,** 207–215.

Tapponnier, P., Peltzer, G., Le Dain, A., Armijo, R. & Cobbold, P., 1982. Propagating extrusion tectonics in Asia: new insights from simple experiments with plasticine, *Geology,* **10**(12), 611–616.

Thielicke, W., 2014, The flapping flight of birds: analysis and application, *PhD thesis,* University of Groningen.

Thielicke, W. & Stamhuis, E., 2014. PIVlab–towards user-friendly, affordable and accurate digital particle image velocimetry in MATLAB, *J. Open Res. Software,* **2**(1), e30, doi:10.5334/jors.bl.

Tikoff, B. & Fossen, H., 1999. Three-dimensional reference deformations and strain facies, *J. Struct. Geol.,* **21**(11), 1497–1512.

van Gelder, I., Willingshofer, E., Sokoutis, D. & Cloetingh, S., 2017. The interplay between subduction and lateral extrusion: a case study for the European Eastern Alps based on analogue models, *Earth planet. Sci. Lett.,* **472,** 82–94.

van Unen, M., Matenco, L., Demir, V., Nader, F.H., Darnault, R. & Mandic, O., 2019. Transfer of deformation during indentation: inferences from the post-middle Miocene evolution of the Dinarides, *Global planet. Change,* **182,** 103027,.

Wallis, D. & Searle, M.P., 2019. Spatial and temporal distributions of deformation in strike-slip faults: the karakoram fault in the india-asia collision zone, in *Transform Plate Boundaries and Fracture Zones,* pp. 271–300, Elsevier.

Wang, L., 1996. A decomposition theorem of motion, *Int. J. Eng. Sci.,* **34**(4), 417–423.

Wang, Y.-Q., Gao, Y.-S., Liu, J.-M. & Liu, C., 2019. Explicit formula for the Liutex vector and physical meaning of vorticity based on the Liutex-Shear decomposition, *J. Hydrodyn.,* **31**(3), 464–474.

White, D., Take, W. & Bolton, M., 2003. Soil deformation measurement using particle image velocimetry (PIV) and photogrammetry, *Geotechnique,* **53**(7), 619–631.

Willingshofer, E. & Sokoutis, D., 2009. Decoupling along plate boundaries: Key variable controlling the mode of deformation and the geometry of collisional mountain belts, *Geology,* **37**(1), 39–42.

Willingshofer, E., Sokoutis, D., Beekman, F., Schönebeck, J., Warsitzka, M., Rosenau, M. & Burg, J., 2018. Ring shear test data of feldspar sand and quartz sand used in the Tectonic Laboratory (TecLab) at Utrecht University for experimental Earth Science applications, *GFZ Data Services,* https://doi.org/10.5880/fidgeo.2018.072 .

Xiao, H., Bruhns, O. & Meyers, A., 1997. Logarithmic strain, logarithmic spin and logarithmic rate, *Acta Mech.,* **124**(1–4), 89–105.

Zheng, Q.-S., He, Q.-C. & Currier, A., 2000. Simple shear decomposition of the deformation gradient, *Acta Mech.,* **140**(3–4), 131–147.

SUPPORTING INFORMATION

Supplementary data are available at *GJI* online.

S1_PIVlab_out_NEMAN SRC 045_video.mov
S2_IncrementalInfinitesimalStrain_video.mp4
S3_LeftStretchV_video.mp4
S4_StrainType_video.mp4

Please note: Oxford University Press is not responsible for the content or functionality of any supporting materials supplied by the authors. Any queries (other than missing material) should be directed to the corresponding author for the paper.

APPENDIX A: SHAPE FUNCTIONS FOR DETERMINING THE DISPLACEMENT GRADIENT

We use linear shape functions to determine the displacement gradient $\frac{\partial \mathbf{u}}{\partial \mathbf{X}}$ for quadrilaterals (deformed rectangles), an approach from finite element analysis to determine deformation of elements. Shape functions provide a convenient method to determine to interpolate nodal quantities, such as displacement, for deformed configurations. First, we define local coordinates $\mathbf{s} = \begin{bmatrix} s & t \end{bmatrix}^T$, shown by Fig. A1.

The global coordinates $\mathbf{x} = \begin{bmatrix} x & y \end{bmatrix}^T$ in the current configuration are related to nodal coordinates $\mathbf{x}_n = \begin{bmatrix} \mathbf{x}_1 & \mathbf{x}_2 & \mathbf{x}_3 & \mathbf{x}_4 \end{bmatrix}$ by:

$$\mathbf{x}(s, t) = \mathbf{x}_n \mathbf{N}(s, t) \tag{A1}$$

local coordinates   global coordinates
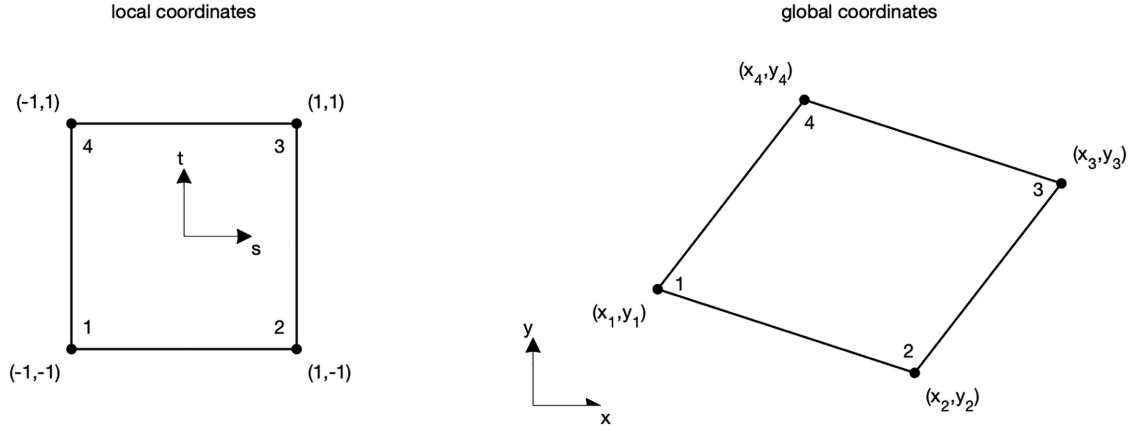

Figure A1. Element definitions: node numbering and coordinate systems. Left panel: element in local coordinates **s**, where the element, even in deformed state, retains its rectangular shape. Right panel: the same element in global coordinates **x**. Nodal coordinates relate to global coordinates as $\mathbf{x} = \mathbf{x}_n N(s, t)$.

with bilinear shape functions **N** (Hughes 2012):

$$
\mathbf{N} = \frac{1}{4}\begin{bmatrix} (1-s)(1-t) \\ (1+s)(1-t) \\ (1+s)(1+t) \\ (1-s)(1+t) \end{bmatrix}
\tag{A2}
$$

For the validity of the bilinear shape functions the requirement holds that all angles between the element sides need to be less than $180°$, which in practice means elements should be sufficiently small to prevent occurrence of angles larger than $180°$. Our elements are isoparametric, which means that the shape functions not only interpolate the coordinates, but serve also as interpolation functions for other nodal quantities, such as displacement.

We have the displacement values $\mathbf{u}_n$ available at each of the four nodal points, and we can interpolate these displacements anywhere within the quadrilateral element using our shape functions **N**:

$$
\mathbf{u}(s, t) = \mathbf{u}_n \mathbf{N}(s, t)
\tag{A3}
$$

where $\mathbf{u} = \begin{bmatrix} u & v \end{bmatrix}^T$ and nodal displacements are:

$$
\mathbf{u}_n = \begin{bmatrix} u_1 & u_2 & u_3 & u_4 \\ v_1 & v_2 & v_3 & v_4 \end{bmatrix}
\tag{A4}
$$

Our main purpose here is to determine $\frac{\partial \mathbf{u}}{\partial \mathbf{X}}$, that we can write as:

$$
\frac{\partial \mathbf{u}}{\partial \mathbf{X}} = \begin{bmatrix} \frac{\partial u}{\partial X} & \frac{\partial u}{\partial Y} \\ \frac{\partial v}{\partial X} & \frac{\partial v}{\partial Y} \end{bmatrix} = \frac{\partial \mathbf{u}}{\partial \mathbf{s}}\frac{\partial \mathbf{s}}{\partial \mathbf{X}} = \begin{bmatrix} \frac{\partial u}{\partial s} & \frac{\partial u}{\partial t} \\ \frac{\partial v}{\partial s} & \frac{\partial v}{\partial t} \end{bmatrix}\begin{bmatrix} \frac{\partial s}{\partial X} & \frac{\partial s}{\partial Y} \\ \frac{\partial t}{\partial X} & \frac{\partial t}{\partial Y} \end{bmatrix}
\tag{A5}
$$

We do not have access to $\frac{\partial \mathbf{s}}{\partial \mathbf{X}}$ but can compute $\frac{\partial \mathbf{X}}{\partial \mathbf{s}}$ using the shape functions. These two gradients are related as (Hughes 2012):

$$
\frac{\partial \mathbf{s}}{\partial \mathbf{X}} = \left(\frac{\partial \mathbf{X}}{\partial \mathbf{s}}\right)^{-1}
\tag{A6}
$$

Such that the displacement gradient becomes:

$$
\frac{\partial \mathbf{u}}{\partial \mathbf{X}} = \begin{bmatrix} \frac{\partial u}{\partial s} & \frac{\partial u}{\partial t} \\ \frac{\partial v}{\partial s} & \frac{\partial v}{\partial t} \end{bmatrix}\begin{bmatrix} \frac{\partial X}{\partial s} & \frac{\partial X}{\partial t} \\ \frac{\partial Y}{\partial s} & \frac{\partial Y}{\partial t} \end{bmatrix}^{-1}
\tag{A7}
$$

We can thus compute the displacement gradient as the product of the displacement gradient with respect to the local coordinates, and the inverse of the gradient of the global coordinates **X** to the local coordinates $\frac{\partial \mathbf{X}}{\partial \mathbf{s}}$, which is often called the jacobian **J**. Using eq. (A3) we compute the elements of $\frac{\partial \mathbf{u}}{\partial \mathbf{s}}$ at the centroid of the element ($s = 0, t = 0$):

$$
\frac{\partial \mathbf{u}}{\partial \mathbf{s}} = \mathbf{u}_n \frac{\partial \mathbf{N}}{\partial \mathbf{s}}
\tag{A8}
$$

Furthermore, the partial derivatives of the shape functions are (at the centroid):

$$
\frac{\partial \mathbf{N}}{\partial s} = \frac{1}{4}\begin{bmatrix} t-1 \\ 1-t \\ 1+t \\ -1-t \end{bmatrix} \qquad \frac{\partial \mathbf{N}}{\partial s}\Big|_{0,0} = \frac{1}{4}\begin{bmatrix} -1 \\ 1 \\ 1 \\ -1 \end{bmatrix}
\tag{A9}
$$

$$\frac{\partial \mathbf{N}}{\partial t} = \frac{1}{4}\begin{bmatrix} s-1 \\ s-1 \\ 1+s \\ 1-s \end{bmatrix} \quad \frac{\partial \mathbf{N}}{\partial t}\Big|_{0,0} = \frac{1}{4}\begin{bmatrix} -1 \\ -1 \\ 1 \\ 1 \end{bmatrix} \tag{A10}$$

such that:

$$\frac{\partial \mathbf{u}}{\partial s}\Big|_{0,0} = \frac{1}{4}\begin{bmatrix} -u_1+u_2+u_3-u_4 & -u_1-u_2+u_3+u_4 \\ -v_1+v_2+v_3-v_4 & -v_1-v_2+v_3+v_4 \end{bmatrix} \tag{A11}$$

Subsequently, using eq. (A1), $\frac{\partial \mathbf{X}}{\partial s}$ is:

$$\frac{\partial \mathbf{X}}{\partial s} = \begin{bmatrix} \mathbf{X}_n \frac{\partial \mathbf{N}}{\partial s} & \mathbf{X}_n \frac{\partial \mathbf{N}}{\partial t} \\ \mathbf{Y}_n \frac{\partial \mathbf{N}}{\partial s} & \mathbf{Y}_n \frac{\partial \mathbf{N}}{\partial t} \end{bmatrix} \tag{A12}$$

evaluated at the centroid, using eq. (A9) again:

$$\frac{\partial \mathbf{X}}{\partial s}\Big|_{0,0} = \frac{1}{4}\begin{bmatrix} -X_1+X_2+X_3-X_4 & -X_1-X_2+X_3+X_4 \\ -Y_1+Y_2+Y_3-Y_4 & -Y_1-Y_2+Y_3+Y_4 \end{bmatrix} \tag{A13}$$

Finally, we can determine the displacement gradient at the centroid by combining eqs A7, A11 and A13

$$\frac{\partial \mathbf{u}}{\partial \mathbf{X}}\Big|_{0,0} = \frac{1}{4}\begin{bmatrix} -u_1+u_2+u_3-u_4 & -u_1-u_2+u_3+u_4 \\ -v_1+v_2+v_3-v_4 & -v_1-v_2+v_3+v_4 \end{bmatrix}. \tag{A14}$$

$$4\begin{bmatrix} -X_1+X_2+X_3-X_4 & -X_1-X_2+X_3+X_4 \\ -Y_1+Y_2+Y_3-Y_4 & -Y_1-Y_2+Y_3+Y_4 \end{bmatrix}^{-1} \tag{A15}$$

As a last note on the determination of $\mathbf{F}$: any deformation described of an element that is initially square leads to parallel orientation of opposing quadrilateral sides when using $\mathbf{F}$. In general deformed quadrilaterals will not have exactly parallel orientations. Deformation of the quadrilaterals as obtained from eq. (1), will then start to deviate from displacement that can be calculated using $\mathbf{F}$. Still $\mathbf{F}$ will hold for the centroid of the quadrilateral. To minimize differences between the quadrilateral deformation and that described by $\mathbf{F}$ the elements should be chosen sufficiently small.

APPENDIX B: POLAR DECOMPOSITION OF THE DEFORMATION GRADIENT IN 2D

Analytic solutions exist for the decomposition of the deformation gradient $\mathbf{F}$ into the rotation tensor $\mathbf{R}$ and the right stretch tensor $\mathbf{U}$ as well as the left stretch tensor $\mathbf{V}$ (Hoger & Carlson 1984). As the polar decomposition holds:

$$\mathbf{F} = \mathbf{RU} = \mathbf{VR} \tag{B1}$$

Knowledge on $\mathbf{U}$ and $\mathbf{U}^{-1}$ leads to $\mathbf{V}$ and $\mathbf{R}$ (recall that $\mathbf{RR}^T = \mathbf{I}$) by:

$$\mathbf{R} = \mathbf{FU}^{-1} \qquad \mathbf{V} = \mathbf{FR}^T \tag{B2}$$

Hoger & Carlson (1984) provide expressions for $\mathbf{U}$ in closed form as well as its inverse, without the need to determine the tensor square root of the right Cauchy-Green tensor $\mathbf{C}$, as $\mathbf{U} = \sqrt{\mathbf{C}}$.

Firstly the principal values μ of $\mathbf{C}$:

$$\mu_1 = \frac{C_{11}+C_{22}+\sqrt{(C_{11}-C_{22})^2+4C_{12}^2}}{2} \tag{B3}$$

$$\mu_2 = \frac{C_{11}+C_{22}-\sqrt{(C_{11}-C_{22})^2+4C_{12}^2}}{2} \tag{B4}$$

From these the invariants of $\mathbf{C}$ and $\mathbf{U}$ can be calculated:

$$I_C = \mu_1 + \mu_2 \qquad II_C = \mu_1\mu_2 \tag{B5}$$

$$I_U = \sqrt{I_C + 2\sqrt{II_C}} \qquad II_U = \sqrt{II_C} \tag{B6}$$

By inserting B3 into B5 we can further simplify the invariants and bypass the computation of principal values:

$$I_C = C_{11}+C_{22} \qquad II_C = C_{11}C_{22} - C_{12}^2 \tag{B7}$$

Then the right stretch tensor is:

$$\mathbf{U} = (\mathbf{C} + II_U\mathbf{I})/I_U \tag{B8}$$

and its inverse:

$$\mathbf{U}^{-1} = -I_U \frac{\mathbf{C} - (II_U + I_C)\mathbf{I}}{II_U(II_U + I_C) + II_C} \tag{B9}$$

Which we can insert in eq. (B2) again to obtain **V** and **R**. The rotation angle θ represented by **R** can be calculated using the four-quadrant inverse tangent:

$$\theta = atan2(R_{21}, R_{11}) \tag{B10}$$